





















## ALMA observations of NGC 6334S. II. Subsonic and Transonic Narrow Filaments in a High-mass Star Formation Cloud

SHANGHUO LI <sup>1</sup>, PATRICIO SANHUEZA <sup>2,3</sup>, CHANG WON LEE <sup>1,4</sup>, QIZHOU ZHANG <sup>5</sup>, HENRIK BEUTHER <sup>6</sup>,  
AINA PALAU <sup>7</sup>, HONG-LI LIU<sup>8</sup>, HOWARD SMITH<sup>5</sup>, HAUYU BAOBAB LIU <sup>9</sup>, IZASKUN, JIMÉNEZ-SERRA <sup>10</sup>,  
KEE-TAE KIM <sup>1,4</sup>, SIYI FENG <sup>11,12,13</sup>, TIE LIU <sup>14</sup>, JUNZHI WANG <sup>14</sup>, DI LI <sup>11,15</sup>, KEPING QIU <sup>16</sup>, XING LU <sup>14,2</sup>,  
JOSEP MIQUEL GIRART <sup>17</sup>, KE WANG <sup>18</sup>, FEI LI <sup>16</sup>, JUAN LI <sup>14</sup>, YUE CAO<sup>16,5</sup>, SHINYOUNG KIM <sup>1,4</sup> AND  
SHAYE STROM<sup>5</sup>

<sup>1</sup>*Korea Astronomy and Space Science Institute, 776 Daedeokdae-ro, Yuseong-gu, Daejeon 34055, Republic of Korea*

<sup>2</sup>*National Astronomical Observatory of Japan, National Institutes of Natural Sciences, 2-21-1 Osawa, Mitaka, Tokyo 181-8588, Japan*

<sup>3</sup>*Department of Astronomical Science, SOKENDAI (The Graduate University for Advanced Studies), 2-21-1 Osawa, Mitaka, Tokyo 181-8588, Japan*

<sup>4</sup>*University of Science and Technology, 217 Gajeong-ro, Yuseong-gu, Daejeon 34113, Republic of Korea*

<sup>5</sup>*Center for Astrophysics | Harvard & Smithsonian, 60 Garden Street, Cambridge, MA 02138, USA*

<sup>6</sup>*Max Planck Institute for Astronomy, Königstuhl 17, 69117 Heidelberg, Germany*

<sup>7</sup>*Instituto de Radioastronomía y Astrofísica, Universidad Nacional Autónoma de México, P.O. Box 3-72, 58090, Morelia, Michoacán, México*

<sup>8</sup>*Department of Astronomy, Yunnan University, Kunming, 650091, People's Republic of China*

<sup>9</sup>*Academia Sinica Institute of Astronomy and Astrophysics, 11F of AS/NTU Astronomy-Mathematics Building, No.1, Sec. 4, Roosevelt Road, Taipei 10617, Taiwan*

<sup>10</sup>*Centro de Astrobiología (CSIC-INTA), Carretera de Ajalvir, Km. 4, Torrejón de Ardoz, 28850 Madrid, Spain*

<sup>11</sup>*National Astronomical Observatories, Chinese Academy of Sciences, Beijing 100101, People's Republic of China*

<sup>12</sup>*Academia Sinica Institute of Astronomy and Astrophysics, 11F of AS/NTU Astronomy-Mathematics Building, No.1, Sec. 4, Roosevelt Road, Taipei 10617, Taiwan*

<sup>13</sup>*National Astronomical Observatory of Japan, 2-21-1 Osawa, Mitaka, Tokyo, 181-8588, Japan*

<sup>14</sup>*Shanghai Astronomical Observatory, Chinese Academy of Sciences, 80 Nandan Road, Shanghai 200030, People's Republic of China*

<sup>15</sup>*NAOC-UKZN Computational Astrophysics Centre, University of KwaZulu-Natal, Durban 4000, South Africa*

<sup>16</sup>*School of Astronomy and Space Science, Nanjing University, 163 Xianlin Avenue, Nanjing 210023, People's Republic of China*

<sup>17</sup>*Institut de Ciències de l'Espai (IEEC-CSIC), Campus UAB, Carrer de Can Magrans s/n, 08193 Cerdanyola del Vallès, Catalonia, Spain*

<sup>18</sup>*Kavli Institute for Astronomy and Astrophysics, Peking University, 5 Yiheyuan Road, Haidian District, Beijing 100871, People's Republic of China*

### ABSTRACT

We present a study of narrow filaments toward a massive infrared dark cloud, NGC 6334S, using the Atacama Large Millimeter/submillimeter Array (ALMA). Thirteen gas filaments are identified using the H<sup>13</sup>CO<sup>+</sup> line, while a single continuum filament is revealed by the continuum emission. The filaments present a compact radial distribution with a median filament width of  $\sim 0.04$  pc narrower than the previously proposed ‘quasi-universal’ 0.1 pc filament width. The higher spatial resolution observations and higher-density gas tracer tend to identify even narrower and lower mass filaments. The filament widths are roughly twice the size of embedded cores. The gas filaments are largely supported by thermal motions. The nonthermal motions are predominantly subsonic and transonic in both identified gas filaments and embedded cores, which may imply that stars are likely born in environments of low turbulence. A fraction of embedded objects show a narrower velocity dispersion compared with their corresponding natal filaments, which may indicate that the turbulent dissipation is taking place in these embedded cores. The physical properties (mass, mass per unit length, gas kinematics, and width) of gas filaments are analogous to those of narrow filaments found in low- to high-mass star-forming regions. The more evolved sources are found to be farther away from the

filaments, a situation that may have resulted from the relative motions between the YSOs and their natal filaments.

*Keywords:* Interstellar filaments (842), Protoclusters (1297), Interstellar medium (847), Interstellar line emission (844), Star formation (1569), Star forming regions (1565), Early-type stars (430), Infrared dark clouds (787)

## 1. INTRODUCTION

Filamentary structures of interstellar medium (ISM) are prevalent in nearby Gould Belt molecular clouds and also more distant molecular clouds as seen in recent Galactic plane surveys from far-infrared to centimeter wavelengths and in both continuum and molecular line emission (Churchwell et al. 2009; André et al. 2010; Molinari et al. 2010; Arzoumanian et al. 2011; Goodman et al. 2014; Wang et al. 2015; Zucker et al. 2015; Contreras et al. 2016; Li et al. 2016; Soler et al. 2020; Wang et al. 2020). These filaments show wide ranges of physical properties (e.g., length, width, mass, length-to-width aspect ratios, and masses per unit length) that can vary over an order of magnitude across the revealed filaments.

Similar filamentary structures are also commonly seen in both numerical hydrodynamic (HD) and magneto-hydrodynamic (MHD) simulations of the ISM (e.g., Padoan et al. 2007; Heitsch et al. 2008; Gong & Ostriker 2011; Hennebelle 2013; Gómez & Vázquez-Semadeni 2014). Several mechanisms have been proposed for the formation of filaments in molecular clouds, such as gravitational instability (gravitational fragmentation and collapse) of sheet-like and elongated clouds (Miyama et al. 1987; Nagai et al. 1998; Hartmann & Burkert 2007; Hennebelle 2013; Gómez & Vázquez-Semadeni 2014; Van Loo et al. 2014), cloud collision (Padoan et al. 2001), and shocked flows (Gong & Ostriker 2011; Chen et al. 2020).

In dense and self-gravitating clouds, filaments often exhibit cylindrical morphologies. (e.g., Taurus B213; Li & Goldsmith 2012). Large scale filaments often harbor parsec-scale dense massive clumps that become the fertile ground of massive star and cluster formation (Zhang et al. 2009; Jiménez-Serra et al. 2014; Wang et al. 2014; Busquet et al. 2016), although not all filaments show signs of star-formation activity (e.g., only pre-stellar cores are detected in Polaris flare; Miville-Deschênes et al. 2010). The embedded dense cores that are precursors of stars can be formed in the highest density regions of the filament via contraction by self-gravity and local kinematic processes (Inutsuka & Miyama 1992; Hartmann & Burkert 2007; Heitsch et al. 2008, 2009; Nakamura & Li 2008; Myers 2009; Gong & Ostriker 2011). The prestellar cores and protostel-

lar cores are primarily found to reside in dense filamentary structures with supercritical mass per unit length in both low- and high-mass star-forming molecular clouds (André et al. 2014; Chung et al. 2019; Treviño-Morales et al. 2019), and most of them are believed to have formed by cloud collapse and/or fragmentation along filaments (Men’shchikov et al. 2010; André et al. 2014; Henshaw et al. 2014; Peretto et al. 2014; Beuther et al. 2015; Könyves et al. 2015; Clarke et al. 2017). The gas flows along filaments can continuously supply the material for cores to grow in mass (Liu et al. 2012; Kirk et al. 2013; Lin et al. 2017; Yuan et al. 2018; Lu et al. 2018; Liu et al. 2019; Treviño-Morales et al. 2019; Sanhueza et al. 2021).

Recently, ALMA high angular resolution observations reveal that narrow (i.e., filament widths of a few 0.01 pc) filamentary structures (or “fibers” in Hacar et al. 2018), are found in some high-mass star-forming clouds (e.g., Orion, G035.39-00.33, and G14.225-0.506; Henshaw et al. 2014; Hacar et al. 2018; Monsch et al. 2018; Chen et al. 2019b, and references therein). These filaments are much narrower than the ‘quasi-universal’ 0.1 pc filament width proposed by previous studies using *Herschel* observations (e.g., André et al. 2014; Arzoumanian et al. 2019, and references therein), and appear to be intimately linked to dense cores (Hacar et al. 2018). However, whether such narrow filamentary structures are ubiquitous in high-mass star formation clouds, and what their properties are remain controversial topics to be more fully explored.

To understand the nature of filaments and embedded dense cores in massive star formation regions, we have carried out high angular resolution observations toward a filamentary infrared dark cloud, NGC 6334S, using the Atacama Large Millimeter/submillimeter Array (ALMA). NGC 6334S is located at the southwestern end of the NGC 6334 molecular cloud complex (Figure 1), which is a nearby (1.3 kpc) young and massive “mini-starburst” region (Chibueze et al. 2014; Willis et al. 2013). In contrast to the well-known infrared bright OB cluster-forming clumps NGC 6334I/I(N)/II/III/IV/V (Persi & Tapia 2008; Russeil et al. 2013), NGC 6334S in some areas is dark in the infrared at wavelengths up to 70  $\mu\text{m}$  (see Figure 1 of Li et al. 2020a, hereafter Paper I), signalling its youth. NGC 6334S has a mass

of  $\sim 1390 M_{\odot}$  (Paper I), which is comparable to the clumps with embedded massive protostars and proto-clusters elsewhere in the complex, and therefore has the potential to form massive stars together with lower-mass star clusters. Thus NGC 6334S provides an ideal laboratory to investigate the early evolutionary stages of cluster formation in filamentary clouds. We will use dense gas tracers and continuum emission not only to identify the filamentary structures in the position-position-velocity (PPV) space but also to study the physical properties (e.g., gas kinematics, mass, structure profile) of both filaments and dense cores, in order to understand the initial cloud environment of filament-based cluster formation.

We recently identified 49 continuum dense cores (hereafter continuum cores, named respectively #1, #2, #3 ...) using our 3 mm continuum image (Paper I) and found 17 starless cores (hereafter  $\text{NH}_2\text{D}$  cores, namely M1, M2, M3 ...) using the  $\text{NH}_2\text{D}$  line emission (Li et al. 2021, hereafter Paper II). These  $\text{NH}_2\text{D}$  cores are neither associated with continuum cores nor with Class I/II young stellar objects (YSOs; Willis et al. 2013). For simplicity, we refer to continuum cores and  $\text{NH}_2\text{D}$  cores as dense cores. The derived masses of dense cores range from 0.13 to 14.1  $M_{\odot}$ , with the mean and median values of 1.8 and 0.8  $M_{\odot}$ , respectively. The sizes of dense cores are between 0.01 and 0.04 pc, with the mean and median values of 0.018 and 0.017 pc, respectively. Paper I also shows that the nonthermal motions are predominantly subsonic and transonic throughout NGC 6334S and that the external pressure is important in confining the embedded objects. Paper II reported the presence of a cluster of low-mass starless and pre-stellar cores that show small velocity dispersions, a high fractional abundance of  $\text{NH}_2\text{D}$ , high  $\text{NH}_3$  deuterium fractionation, and are dark at infrared wavelengths to 70  $\mu\text{m}$ . In at least some of the  $\text{NH}_2\text{D}$  cores, turbulence seems dissipated and the gas kinematics is dominated by thermal motions.

In this work, we focus on filaments and investigate their properties as well as the relationship between filaments and dense cores. The observations are described in Section 2. Then, we describe the filament identification and the properties of identified filaments in Section 3. We discuss in detail the properties of filaments and dense objects in Section 4. Finally, we summarize our main findings in Section 5.

## 2. OBSERVATION

We have carried out a 55-pointings mosaic observation with ALMA 12m array towards the massive infrared dark cloud (IRDC) NGC 6334S between March 13 and

21 of 2017 (ID: 2016.1.00951.S). Two 234.4 MHz wide spectral windows were employed to cover the  $\text{H}^{13}\text{CO}^+$  (1-0, 86.7 GHz) and  $\text{NH}_2\text{D}$  ( $1_{1,1} - 1_{0,1}$ , 85.9 GHz) lines with a 0.061 MHz spectral resolution ( $\sim 0.21 \text{ km s}^{-1}$  at 86 GHz). In addition, three 1.875 GHz wide spectral windows centered at 88.5 GHz, 98.5 GHz, and 100.3 GHz with a spectral resolution of 0.977 MHz ( $\sim 3.0 - 3.3 \text{ km s}^{-1}$ ) were used to take broad band continuum data. More details on the observations can be found in Paper I.

Data calibration was performed using the CASA 4.7.0 software package (McMullin et al. 2007). Both continuum and line images were iteratively cleaned with manual masking via the *clean* task down to  $\sim 3\sigma$  using the multiscale deconvolver and a robust weighting of 0.5. The resultant continuum and line images have a synthesized beam of  $\theta_{\text{maj}} \times \theta_{\text{min}} = 3''.6 \times 2''.4$  (or  $0.023 \times 0.015 \text{ pc}$ , with a position angle  $\text{P.A.} = 81^\circ$ ) and  $\theta_{\text{maj}} \times \theta_{\text{min}} = 4''.1 \times 2''.8$  (or  $0.026 \times 0.018 \text{ pc}$ ,  $\text{P.A.} = 83^\circ$ ), respectively. The achieved  $1\sigma$  root mean square (rms) noise levels are 0.3 mJy beam $^{-1}$  for the continuum image and  $\sim 6 \text{ mJy beam}^{-1}$  per  $0.21 \text{ km s}^{-1}$  for the spectral line images. The maximum recoverable scale (MRS) of single pointing reaches up to  $\sim 30''$  in the ALMA data. All images shown in this paper are prior to primary beam correction. The measured fluxes for mass estimation have the primary beam correction applied.

## 3. RESULTS AND ANALYSIS

NGC 6334S is mostly dark at infrared wavelengths to 70  $\mu\text{m}$  indicating its early evolutionary stage. (e.g., Sanhueza et al. 2013, 2019; Tan et al. 2013; Contreras et al. 2018; Sanhueza et al. 2017; Li et al. 2019a; Morii et al. 2021). Figure 1 shows an overview of the NGC 6334 molecular cloud complex in the far-infrared and the location of NGC 6334S.

### 3.1. Molecular Lines Emission

The rotational transitions of several molecular species (i.e.,  $\text{HCO}^+$  (1-0),  $\text{HCN}$  (1-0),  $\text{CS}$  (2-1),  $\text{HNCO}$  ( $4_{0,4} - 3_{0,3}$ ),  $\text{H}^{15}\text{NC}$  (1-0),  $\text{CH}_3\text{OH}$  ( $5_{1,4} - 4_{1,3}$ ),  $\text{SO}$  ( $2_2 - 1_1$ ),  $\text{HC}_3\text{N}$  (11-10)) were detected with a coarse spectral resolution of 0.977 MHz (or  $\sim 3.0 - 3.3 \text{ km s}^{-1}$ ). However with these low spectral resolution data we are not able to determine the kinematic properties of the molecular gas. Therefore, only the high spectral resolution (0.061 MHz  $\sim 0.21 \text{ km s}^{-1}$ ) data of the  $\text{H}^{13}\text{CO}^+$  (1-0) and  $\text{NH}_2\text{D}$  ( $1_{1,1} - 1_{0,1}$ ) lines will be used as diagnostics of the kinematic properties of the filaments in this work.

Figures 1 and 2 show the  $\text{H}^{13}\text{CO}^+$  line, continuum, and  $\text{NH}_2\text{D}$  line emission. The  $\text{H}^{13}\text{CO}^+$  (1-0; critical density  $n_{\text{cr}} \sim 10^5 \text{ cm}^{-3}$ ) line traces spatially much more



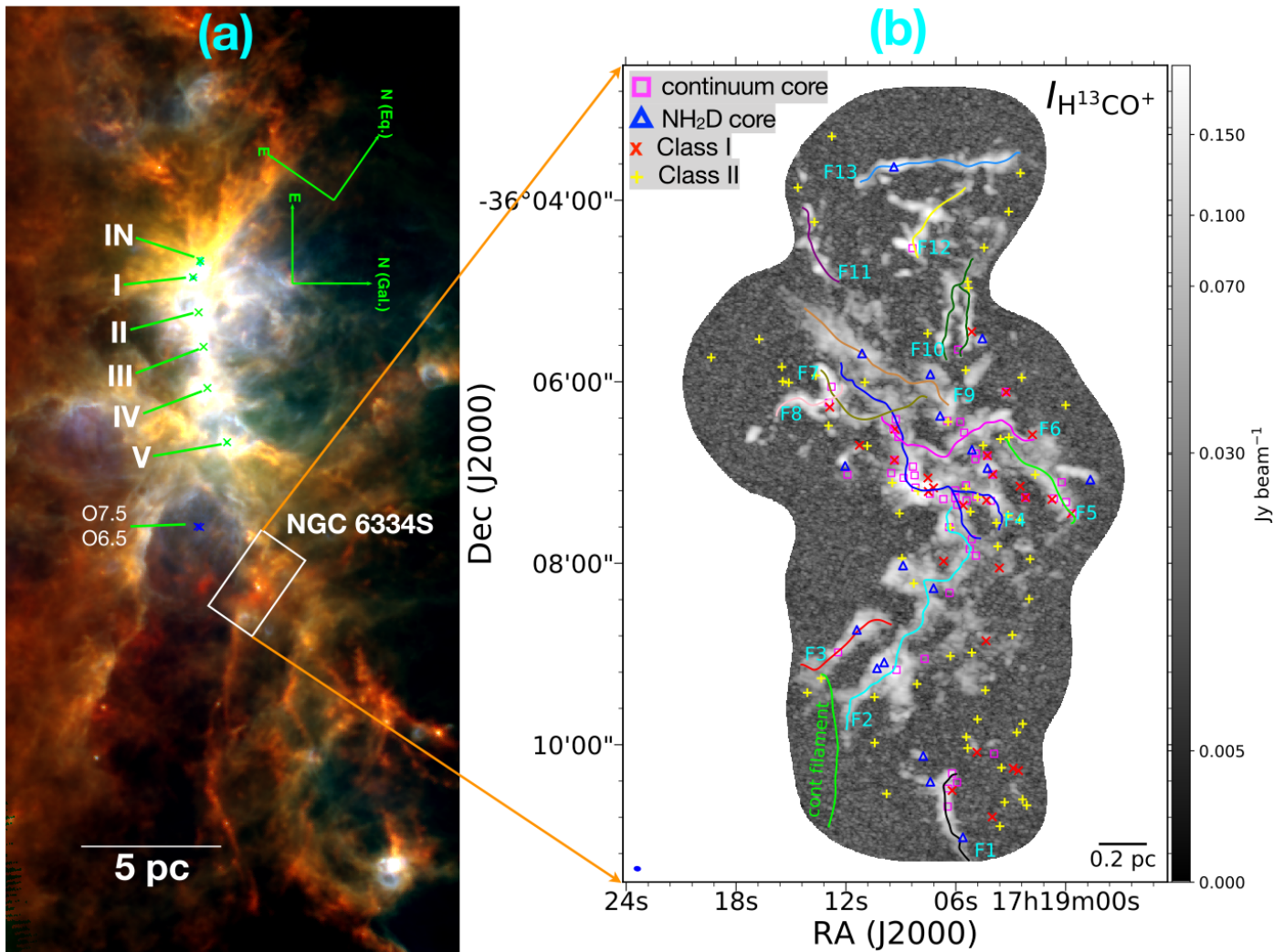


**Figure 1.** Panel a: three-color *Herschel* composite image of NGC 6334 molecular cloud complex with blue, green, and red for  $\lambda = 70, 160,$  and  $350 \mu\text{m}$ , respectively. The scale bar (5 pc at the distance of 1.3 kpc), the Equatorial and the Galactic cardinal directions are shown on the upper right hand of the image. The white box presents the NGC 6334S region. Six bright infrared (IR) clumps (I, IN, II, III, IV, and V) are marked in the image (McBreen et al. 1979). Two O type stars (O7.5 and O6.5) are marked with blue cross “x” symbols (Persi & Tapia 2008). Panel b: the filament spines (color solid curves) overlaid on the peak intensity ( $I_{\text{H}^{13}\text{CO}^+}$ ; the maximum intensity of the spectrum) image of  $\text{H}^{13}\text{CO}^+$  line emission. Magenta open squares correspond to the 49 continuum cores identified by the ALMA 3mm continuum image (Paper I). Blue open triangles show the 17  $\text{NH}_2\text{D}$  cores revealed by the  $\text{NH}_2\text{D}$  line emission (Paper II). The red cross “x” and yellow plus “+” symbols correspond to the 25 Class I and 58 Class II YSOs (Willis et al. 2013), respectively. The beam size (blue filled ellipse) of the  $\text{H}^{13}\text{CO}^+$  image is shown in the bottom left of the panel.

242 extended gaseous structures than the  $\text{NH}_2\text{D}$  ( $1_{1,1} - 1_{0,1}$ ;  
 243  $n_{\text{cr}} \sim 10^6 \text{ cm}^{-3}$ ) line since their critical densities are  
 244 different by nearly an order-of-magnitude. The  $\text{NH}_2\text{D}$   
 245 emission appears preferentially toward the location of  
 246 dense cores. In addition, the  $\text{H}^{13}\text{CO}^+$  emission is in  
 247 a better agreement with the *Spitzer* dark and *Herschel*  
 248 bright filamentary structures than that of  $\text{NH}_2\text{D}$  (see  
 249 also Paper I). These all suggest that the  $\text{H}^{13}\text{CO}^+$  emis-  
 250 sion is a better tracer of filamentary structures than  
 251  $\text{NH}_2\text{D}$ . In what follows, the  $\text{H}^{13}\text{CO}^+$  will be therefore  
 252 used to identify the velocity-coherent filamentary struc-

253 tures. There is the continuum filamentary structure in  
 254 the south-eastern part of the map (see Figures 1 and  
 255 2), which continuum emission is unlikely dominated by  
 256 dust emission (See discussions below in Section 4.1).

257 We used the  $\sim 7''$  resolution  $\text{NH}_3$  rotational tempera-  
 258 tures ( $T_{\text{NH}_3}$ ) derived in paper I. For the regions where  
 259 the  $\text{NH}_3$  data are not available, we assume a gas kinem-  
 260 atic temperature of  $\langle T_{\text{NH}_3} \rangle = 15 \text{ K}$ , the average gas  
 261 temperature derived from the observed  $\text{NH}_3$  data.

### 3.2. Velocity Structures



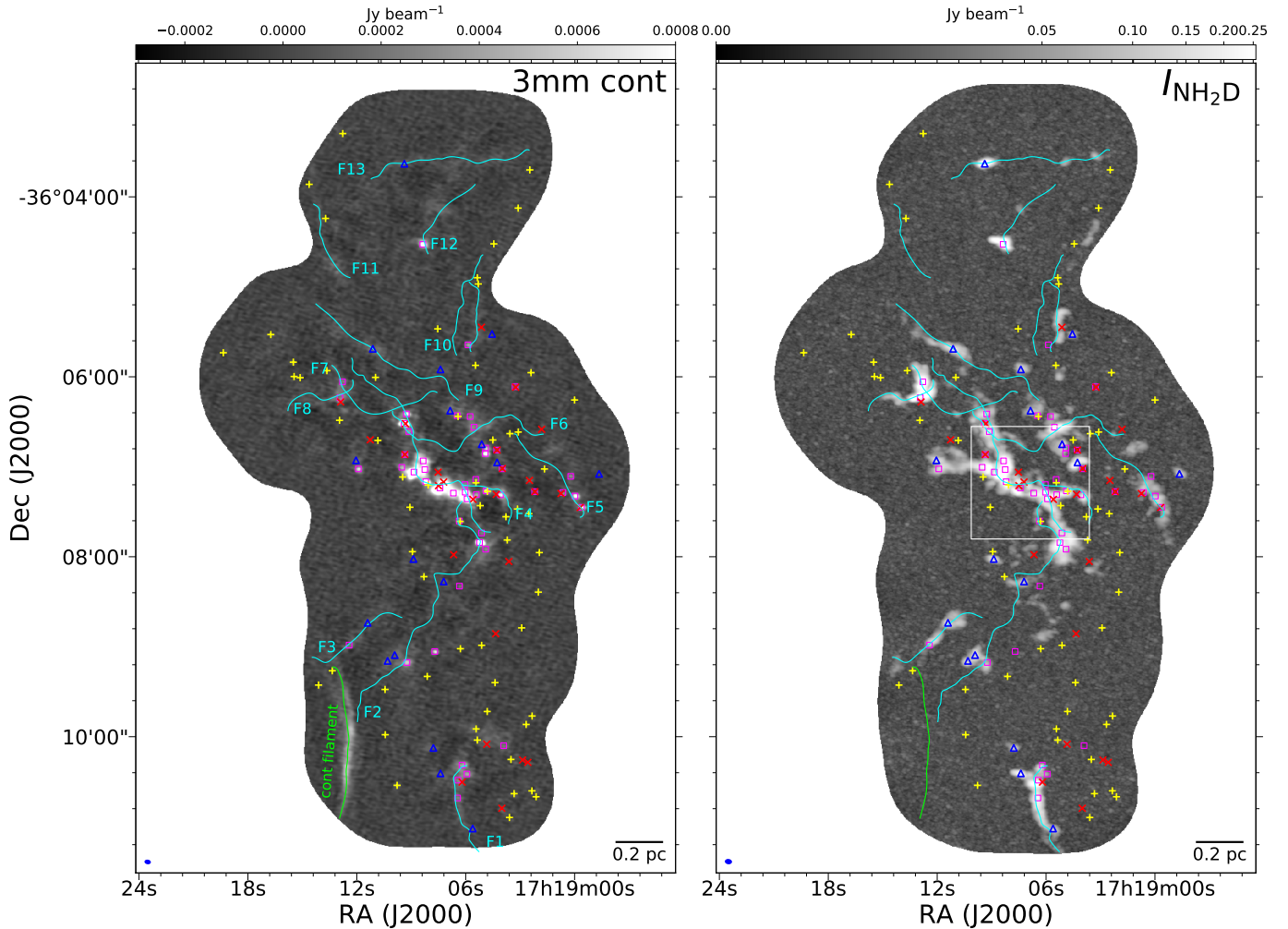


**Figure 2.** Magenta open squares, blue open triangles, red cross “x”, and yellow plus “+” symbols show the continuum cores, NH<sub>2</sub>D cores, Class I, and Class II, respectively. Left: the filament spines (cyan and green solid curves) overlaid on the 3 mm continuum image. Right: the filament spines (cyan and green solid curves) overlaid on the peak intensity map ( $I_{\text{NH}_2\text{D}}$ ) of the NH<sub>2</sub>D line emission. White box shows the region where outflows are identified, with zoomed-in views presented in Figures 9. The beam size is shown in the bottom left of each panel.

263 Paper I found that multiple velocity components  
 264 were detected in some areas where significant H<sup>13</sup>CO<sup>+</sup>  
 265 emission was detected. Since the majority (~85%)  
 266 of H<sup>13</sup>CO<sup>+</sup> emission appears as a single velocity  
 267 component, we show the intensity-weighted velocity  
 268 (1st-moment) and intensity-weighted dispersion (2nd-  
 269 moment) of the H<sup>13</sup>CO<sup>+</sup> line emission in Figure 3. We  
 270 note that there are complex velocity structures across  
 271 NGC 6334S, especially toward the central region which  
 272 appears to be associated with multiple velocity compo-  
 273 nents.

274 We fit Gaussian line profiles to the H<sup>13</sup>CO<sup>+</sup> data pixel  
 275 by pixel with multiple velocity components, under the  
 276 assumption that the H<sup>13</sup>CO<sup>+</sup> emission is optically thin.  
 277 The detailed fitting process of molecular lines is summa-  
 278 rized in the Paper I. The observed velocity dispersions

279 ( $\sigma_{\text{obs}}$ ) derived from the Gaussian fitting are between  
 280 0.10 and 0.80 km s<sup>-1</sup>, with mean and median values  
 281 of 0.23 and 0.20 km s<sup>-1</sup>, respectively. The observed  
 282  $\sigma_{\text{obs}}$  is composed of the thermal and nonthermal compo-  
 283 nents. Paper I shows that the nonthermal velocity  
 284 dispersion  $\sigma_{\text{nth}}$  is dominated by subsonic and transonic  
 285 motions throughout NGC 6334S. The  $\sigma_{\text{obs}}$  of the dense  
 286 cores is greater than in the quiescent regions; the  $\sigma_{\text{nth}}$   
 287 and the  $\sigma_{\text{obs}}$  toward the central region of NGC 6334S,  
 288 have generally larger values than that measured in the  
 289 outer regions (see Paper I).

### 3.3. Filament Identification

#### 3.3.1. Friend-of-Friend Algorithm

290  
 291  
 292 The results from the Gaussian fitting as described  
 293 above in Section 3.2 were used to identify gas fila-

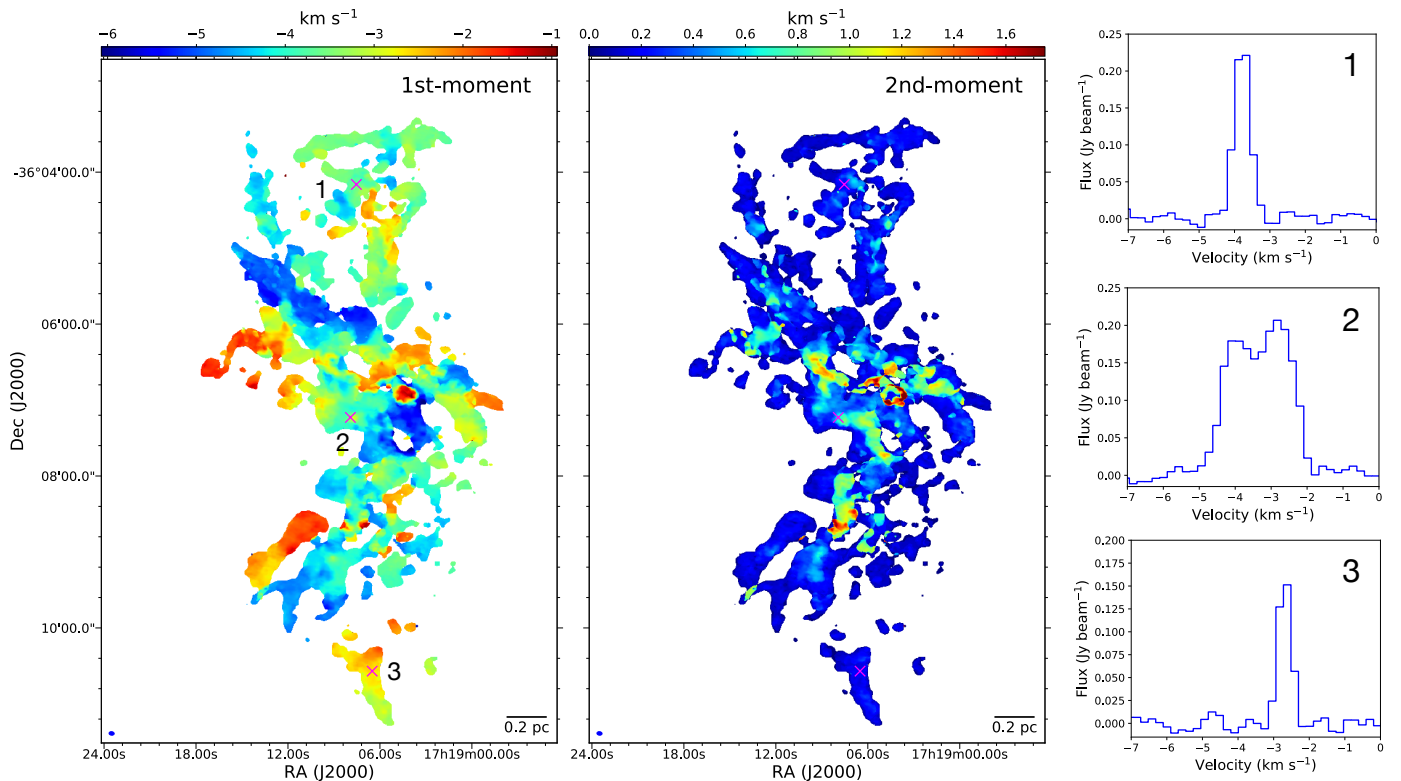


**Figure 3.** Left and middle panels show the H<sup>13</sup>CO<sup>+</sup> intensity-weighted velocity (1st-moment) and intensity-weighted dispersion (2nd-moment) maps, respectively. The beam size is shown in the bottom left of each panel. Right panel shows the spectra of H<sup>13</sup>CO<sup>+</sup> extracted from positions 1, 2, and 3. Three selected positions are marked with red cross “x” in both left and middle panels.

294 ments. Following similar procedures as Hacar et al.  
 295 (2013, 2018), we used the python-based friend-of-friend  
 296 (fof) algorithm<sup>1</sup> (Huchra & Geller 1982) to identify the  
 297 velocity-coherent filaments, i.e., no abrupt change of  
 298 sign of the gradient along the filament in PPV space.

299 We first used the fof algorithm to identify the seed  
 300 points, those that have peak intensities ( $I$ , the maxi-  
 301 mum intensity of the spectrum) above a certain thresh-  
 302 old  $I_0$  ( $7\sigma$ ), of each individual structure. In total, about  
 303  $\sim 70\%$  of the data points are above  $I_0$ . The spatial cri-  
 304 terion between nearby points to be considered as friends  
 305 is  $\Delta r \leq 0.023$  pc ( $\sim 1$  beam size linear scale), while  
 306 the velocity criterion uses an adaptive velocity gradient  
 307  $\nabla v_{\text{LSR},i} = \frac{1}{2} \frac{\Delta v_i}{\theta_{\text{FWHM}}}$  similar to the definition in Hacar  
 308 et al. (2018). Here,  $\Delta v_i$  is the line full width half maxi-  
 309 mum (FWHM) of H<sup>13</sup>CO<sup>+</sup> of the  $i$ th pixel and  $\theta_{\text{FWHM}}$   
 310 is the beam size. Only structures that contain more than  
 311 150 data points (the area of a structure larger than 3  
 312 times the beam size) were considered. Second, we ran  
 313 fof again to search for new friend points of each group  
 314 identified in the first step, where the new friend points

315 come from the remaining data points, in which the low  
 316 intensity points ( $\leq I_0$ ) are encompassed; the same spa-  
 317 tial and velocity criteria are used. After the second fof  
 318 run, there are about 20% of points that are not included  
 319 within any group. The majority of them have relatively  
 320 low intensities and/or appear to unaffiliated with the  
 321 identified filaments.

322 We employed the FilFinder<sup>2</sup> algorithm to compute  
 323 the filament spine. The FilFinder package reduces the  
 324 masking area to identify a skeleton that represents the  
 325 topology of the area, using a Medial Axis Transform.  
 326 The masking area is delineated by the spatial distribu-  
 327 tion of the identified filaments; we refer to the derived  
 328 skeletons as the filament spines. The derived filament  
 329 spines are shown in Figure 1. In total, 13 velocity-  
 330 coherent filaments have been identified by the fof al-  
 331 gorithm from the PPV space of H<sup>13</sup>CO<sup>+</sup> data. Fila-  
 332 ments are named F1, F2, F3 ... in order from south to  
 333 north. Filaments F4 and F10 have additional branches  
 334 and they are named as F4b and F10b. The physical

<sup>1</sup> <https://github.com/ShanghuoLi/pyfof>

<sup>2</sup> <https://github.com/e-koch/FilFinder>

lengths of these identified filaments ( $L_{\text{fil}}$ ) range between 0.4 and 1.3 pc.

### 3.3.2. Velocity-Coherent Filaments

The filament spines overlaid on the channel maps of  $\text{H}^{13}\text{CO}^+$  are shown in Figure 4, which shows that the line emission exhibits a filamentary distribution and that the identified filaments are consistent with the majority of the  $\text{H}^{13}\text{CO}^+$  emission. This provides further evidence that the python-based `fof` algorithm can accurately recover the gas filamentary structures that are connected in both velocity and space (see also Figure 5).

Several small regions show significant  $\text{H}^{13}\text{CO}^+$  emission but are not grouped into any identified filament. For instance, there is a small  $\text{H}^{13}\text{CO}^+$  emission region on the west of F2 at velocity range of between  $-4.20$  and  $3.78 \text{ km s}^{-1}$ , which is marked with red arrows in Figure 4. Two separated substructures appear in this small region, implying the emission is not connected in the spatial space. There are also some isolated small regions separated from the identified filaments in spatial space. These isolated regions fail to be considered as an independent filament because their emission is too weak and/or the number of total data points are lower than the criteria of identification. We stress that the identified filaments are likely to be incomplete. Potential low density and diffuse molecular filamentary structures could have been missed if their  $\text{H}^{13}\text{CO}^+$  line emission is not significant and/or the detection suffers from severe missing flux.

The  $\text{H}^{13}\text{CO}^+$  line emission of identified filaments generally spans  $\geq 4$  channels (a velocity range of  $\geq 0.84 \text{ km s}^{-1}$ ). The filament with the largest spread in velocity is F4, which spans from  $-6.52$  to  $-2.3 \text{ km s}^{-1}$ . The majority of the filaments are spatially distinct, while several filaments partly overlap in position, such as F2–F4, F4–F6, F4–F7, and F7–F8. The overlapping regions tend to show complex velocity structures as characterized by multiple velocity components along the line of sight.

### 3.4. Filament Profile

We employed the `RadFil`<sup>3</sup> package (Zucker & Chen 2018), a radial density profile building and fitting tool for interstellar filaments, to construct the filament radial profile from the velocity integrated intensity of  $\text{H}^{13}\text{CO}^+$  inside the mask of a given filament. We used the `RadFil` tangent to the filament spine at 7 or 8 pixel (about 1 beam size; 1 pixel =  $0''.43$ ) intervals along the filament, then took the radial cut perpendicular to each tangent.

<sup>3</sup> <https://github.com/catherinezucker/radfil>

The radial profile has been shifted along each cut in order to ensure that it is centered on the pixel with the peak intensity. Figure 6 shows the radial cut and the pixels (blue points) of the peak in the radial cut for F1. Along each cut, the radial distance is calculated as the projected distance from the peak intensity. Prior to fitting the profile, the background was subtracted using the background subtraction estimator of `RadFil`. The background is estimated by a first-order polynomial to all profiles at the given radial distance range, and then subtracts it from each cut; the background subtraction radii vary slightly from filament to filament, with a typical range of 0.08–0.15 pc.

To compute the filament widths (FWHM), we performed a Gaussian fitting to the average profile of the  $\text{H}^{13}\text{CO}^+$  intensity of each filament. The Gaussian function is given by

$$A(r) = A_0 \exp\left(\frac{-(r - \mu)^2}{2\sigma_G^2}\right), \quad (1)$$

where  $r$  is the radial distance,  $A$  is the profile amplitude at the radial distance  $r$ ,  $A_0$  is the amplitude,  $\sigma_G$  is the standard deviation, and  $\mu$  is the mean. Here,  $\mu$  is fixed to zero. The best-fit Gaussian of each filament profile is listed in Table 1. An example of the fit is shown in Figure 6, where the red solid line is the best fit, the black dots correspond to the averaged integrated intensity of  $\text{H}^{13}\text{CO}^+$  and the error bars are the standard deviation of the radial profile of all cuts perpendicular to the filament. The best-fit filament widths range from 0.036 to 0.074 pc, with the mean and median values of 0.046 and 0.045 pc, respectively. We also estimated the beam-deconvolved FWHM with  $\text{FWHM}_{\text{decon}} = \sqrt{\text{FWHM}^2 - \text{FWHM}_{\text{bm}}^2}$ , where  $\text{FWHM}_{\text{bm}}$  is the half-power beam width. The  $\text{FWHM}_{\text{bm}}$  is about  $3''.4$  ( $\sim 0.021$  pc) in our observations. The  $\text{FWHM}_{\text{decon}}$  is between 0.029 and 0.071 pc, with the mean and median values of 0.041 and 0.039 pc, respectively.

In previous studies, observed filaments have been considered as cylindrical structures that can be described by a Plummer-like function of the form (e.g., Nutter et al. 2008; Arzoumanian et al. 2011; Palmeirim et al. 2013; Smith et al. 2014; Liu et al. 2018):

$$\int f dv(r) = \frac{A_0}{\left[1 + \left(\frac{r}{R_{\text{flat}}}\right)^2\right]^{\frac{p-1}{2}}}, \quad (2)$$

where  $\int f dv$  is the integrated intensity,  $A_0$  is the peak profile amplitude,  $R_{\text{flat}}$  is the flattening radius, and  $p$  is the power-law index of the density profile at large radii



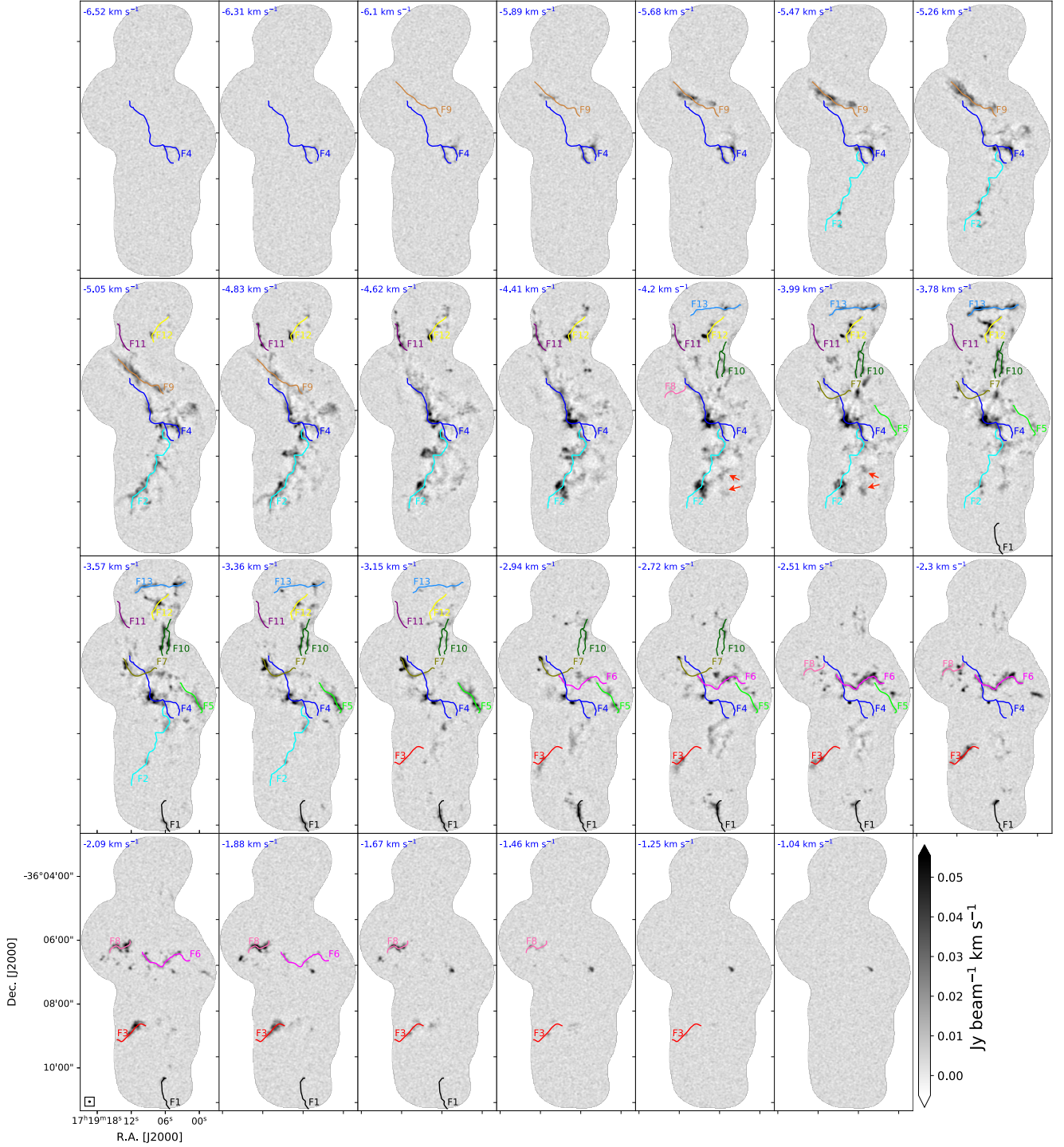


**Figure 4.** The filament spines (solid curves) overlaid on the channel map of  $\text{H}^{13}\text{CO}^+$ . The velocity value is presented in the top left of each panel.

417 (Cox et al. 2016; Zucker & Chen 2018). We also per-  
 418 formed a Plummer fitting to the identified filaments in  
 419 NGC 6334S. The best Plummer fit is shown in dashed  
 420 green line in Figure 6. The filament widths derived by  
 421 the Plummer fitting are similar to those of the Gaus-

422 sian fitting, and FWHM ranges from 0.03 to 0.066 pc,  
 423 with the mean and median values of 0.045 and 0.042  
 424 pc, respectively. The  $\text{FWHM}_{\text{decon}}$  is between 0.023 and  
 425 0.062 pc, with the mean and median values of 0.039 and  
 426 0.037 pc (Table 1), respectively.  $R_{\text{flat}}$  is between

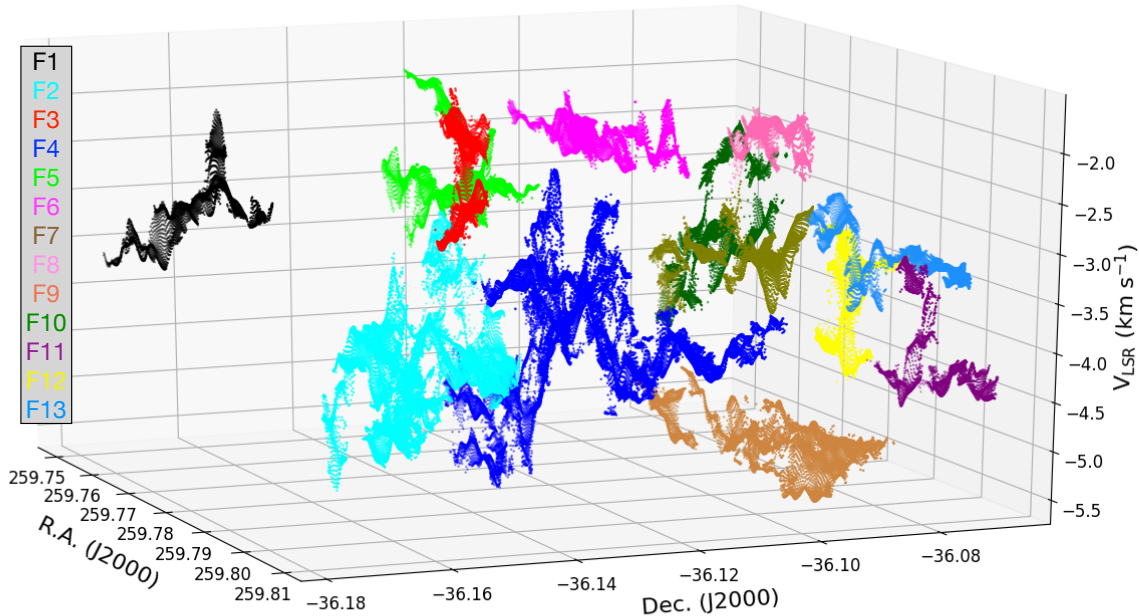


**Figure 5.** Position-position-velocity (PPV) cube shows the centroid velocity of the identified filaments. (The animated version of the PPV cube is available in <https://github.com/ShanghuoLi/NGC6334S-filament>.)

427 and 0.081 pc, with a mean and median values of 0.033  
 428 and 0.027 pc, respectively. Figure 6 shows that some  
 429 of the filament profiles have relatively large dispersions  
 430 due to non-uniform line intensities throughout the fila-  
 431 ments. The significant variations of  $\text{H}^{13}\text{CO}^+$  emission  
 432 across the filaments results in a poor fit in their profiles,  
 433 e.g., F4 and F9.

434 The derived filament widths are similar to those  
 435 of Musca ( $\sim 0.07$  pc; Kainulainen et al. 2016),  
 436 Aquila/Polaris ( $\sim 0.04$  pc; Men'shchikov et al. 2010),  
 437 Orion ( $\sim 0.02 - 0.05$  pc for OMC-1/2 and ISF; Hacar  
 438 et al. 2018), G14.225-0.506 ( $\sim 0.05 - 0.09$  pc; Chen  
 439 et al. 2019b), G035.39-00.33 ( $\sim 0.028$  pc; Henshaw et al.  
 440 2017), and L1287 ( $\sim 0.03$  pc; Sepúlveda et al. 2020).  
 441 In contrast, the derived filament widths are narrower  
 442 than those of *Herschel* filaments studied toward IC 5146  
 443 ( $\sim 0.1$  pc; Arzoumanian et al. 2019), Taurus ( $\sim 0.1$  pc;  
 444 Palmeirim et al. 2013), NGC 6334IN and NGC 6334I  
 445 ( $\sim 0.24$  pc; Russeil et al. 2013). But note that the spa-  
 446 tial resolution of *Herschel* observations (beam size  $\sim$   
 447  $36''$ ) is much poorer than that of the ALMA observa-  
 448 tions. This supports the idea that higher spatial reso-  
 449 lution observations and higher-density gas tracers can  
 450 identify narrower filaments. In addition, the dust con-  
 451 tinuum emission cannot be resolved into separate fila-  
 452 ments when they overlap, whereas velocities measure-  
 453 ments generally can do so. Spatially blended filaments  
 454 might broaden the measured filament widths (see also  
 455 Henshaw et al. 2017). This also indicates that filaments

456 identified with different procedures might show deviat-  
 457 ing filament widths.

### 3.5. Filament Mass

458 The mass per unit length is one important indicator  
 for assessing the stability of filaments. The continuum  
 emission from dust is one of the most frequently used  
 measurement to compute the mass. Figure 2 shows the  
 filament spines overlaid on the 3 mm continuum image.  
 Unfortunately, only 2 gas filaments (F4 and F1) have sig-  
 nificant continuum emission detection (Figure 2); the re-  
 maining 11 gas filaments are either only partly detected  
 in continuum emission or not detected at all above  $5\sigma$ .  
 An alternative way to estimate the filament mass is to  
 make use of molecular gas emission; in this work we use  
 $\text{H}^{13}\text{CO}^+$ . With the fractional abundance of  $\text{H}^{13}\text{CO}^+$   
 relative to  $\text{H}_2$ ,  $X(\text{H}^{13}\text{CO}^+) = N(\text{H}^{13}\text{CO}^+)/N(\text{H}_2)$ , the  
 filament mass can be computed as follows:

$$M_{\text{fil}} = \mu_{\text{H}_2} m_{\text{H}} \sum \frac{N(\text{H}^{13}\text{CO}^+)}{X(\text{H}^{13}\text{CO}^+)} \Omega, \quad (3)$$

459 where  $N(\text{H}^{13}\text{CO}^+)$  is the column density of  $\text{H}^{13}\text{CO}^+$ ,  
 460  $\mu_{\text{H}_2} = 2.8$  is the mean molecular weight of the interstel-  
 461 lar medium (ISM; Kauffmann et al. 2008),  $m_{\text{H}}$  is the  
 462 hydrogen mass, and  $\Omega$  is the solid angle of the  $\text{H}^{13}\text{CO}^+$   
 463 emission. Assuming local thermodynamic equilibrium  
 464 (LTE), the molecular column densities can be esti-  
 465 mated from the velocity-integrated intensity (see Ap-  
 466 pendix A1), and finally leads to  $M_{\text{fil}}$  (see Eq.3).

467 In order to estimate  $X(\text{H}^{13}\text{CO}^+)$  for NGC 6334S,  
 468 we have focused on F4 because both  $\text{H}^{13}\text{CO}^+$  line

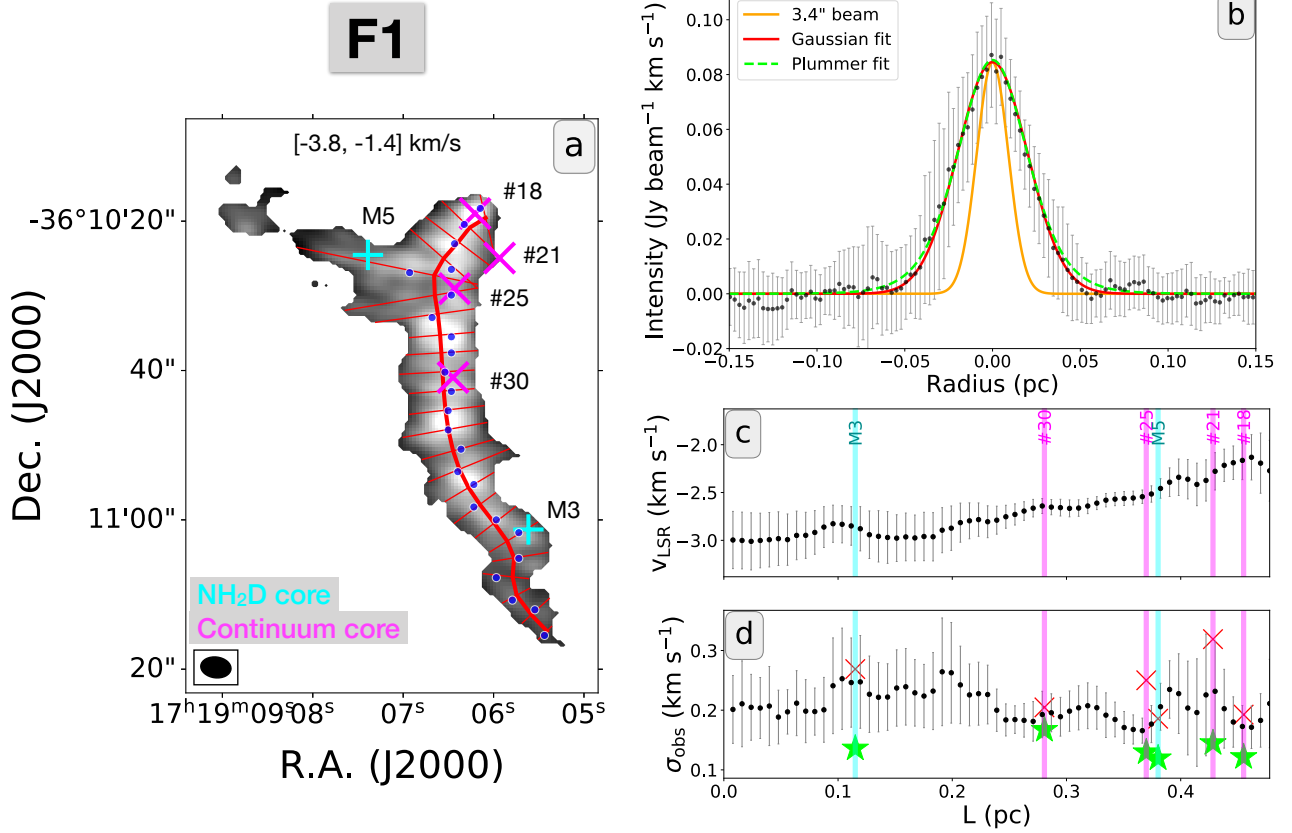


**Figure 6.** Panel a: the filament spine (red solid curves) of F1 overlaid on the velocity-integrated intensity map of  $\text{H}^{13}\text{CO}^+$ . Magenta cross “x” and cyan plus “+” symbols are continuum cores and  $\text{NH}_2\text{D}$  cores, respectively. The velocity range of this filament is presented in the upper middle of the panel. The beam size is shown in the bottom left of the panel. Panel b: mean integrated intensity profile of  $\text{H}^{13}\text{CO}^+$  (black dots) was built by sampling radial cuts (short red solid lines) every 8 pixels (which corresponds to  $3''.44$  or  $\sim 0.019 \text{ pc}$  at the source distance of 1.3 kpc) along the spine. The radial distance is the projected distance from the peak emission at a given cut (blue dots in panel a). The error bar represents the standard deviation of the cuts at each radial distance. The orange solid line shows the beam response with a FWHM of  $\sim 3''.4$ . The red solid and green dashed lines present the best-fit results of Gaussian and Plummer fitting, respectively. Panel c and d: the mean centroid velocity  $\langle v_{\text{LSR}} \rangle$  and mean observed velocity dispersion  $\langle \sigma_{\text{obs}} \rangle$  of  $\text{H}^{13}\text{CO}^+$  line variation along the filament. The error bars show the standard deviation of corresponding  $v_{\text{LSR}}$  and  $\sigma_{\text{obs}}$ . Vertical magenta and cyan lines indicate the positions of associated continuum cores and  $\text{NH}_2\text{D}$  cores, respectively. The red cross “x” and green filled star symbols mark the core mean  $\sigma_{\text{obs}}$  derived from the  $\text{H}^{13}\text{CO}^+$  and  $\text{NH}_2\text{D}$  lines, respectively. The complete figure set (4 images, see Figure 13) is available in the online journal.

and continuum emission are significantly detected (Figures 1 and 2). The derived  $N(\text{H}^{13}\text{CO}^+)$  ranges from  $7.2 \times 10^{11} \text{ cm}^{-2}$  to  $1.4 \times 10^{13} \text{ cm}^{-2}$  and  $N_{\text{H}_2}$  is between  $1.3 \times 10^{22} \text{ cm}^{-2}$  and  $6.1 \times 10^{23} \text{ cm}^{-2}$ . The resulting values of  $X(\text{H}^{13}\text{CO}^+)$  extend from  $7.7 \times 10^{-12}$  to  $3.1 \times 10^{-10}$ , with a median value of  $5.4 \times 10^{-11}$ . The derived  $X(\text{H}^{13}\text{CO}^+)$  is similar to the reported values of  $3.0 \times 10^{-11} - 4.0 \times 10^{-10}$  in Butner et al. (1995),  $4.5 \times 10^{-11}$  in Germer et al. (2014),  $4.8 \times 10^{-10}$  in Sanhueza et al. (2012), and  $1.3 \times 10^{-10}$  in Hoq et al. (2013).

Using the median  $X(\text{H}^{13}\text{CO}^+) = 5.4 \times 10^{-11}$ , we estimated the gas mass ( $M_{\text{fil}}$ ) for each filament. The derived masses are in the range of 4 – 82  $M_{\odot}$  (see Table 1) and the total gas mass in the filaments is about

342  $M_{\odot}$ . The total gas mass estimated from  $\text{H}^{13}\text{CO}^+$  in the observed region is about 395  $M_{\odot}$ , which indicates that these filaments contain most of the dense gas ( $87\% = 342/395$ ), as revealed by the total  $\text{H}^{13}\text{CO}^+$  line emission (see Section 4.5 below). The masses per unit length ( $M_{\text{line}} = M_{\text{fil}}/L_{\text{fil}}$ ) of filaments range between 14 and 64  $M_{\odot} \text{ pc}^{-1}$ , with a median value of 29  $M_{\odot} \text{ pc}^{-1}$  (see Table 1).

The uncertainties in the distance, assumed gas temperature, and variations of the  $\text{H}^{13}\text{CO}^+$  fractional abundance introduce uncertainties in the estimates of the filament masses and masses per unit length. The typical uncertainties in the temperatures derived from  $\text{NH}_3$  is  $\sim 15\%$  (see Paper I). The uncertainty in distance



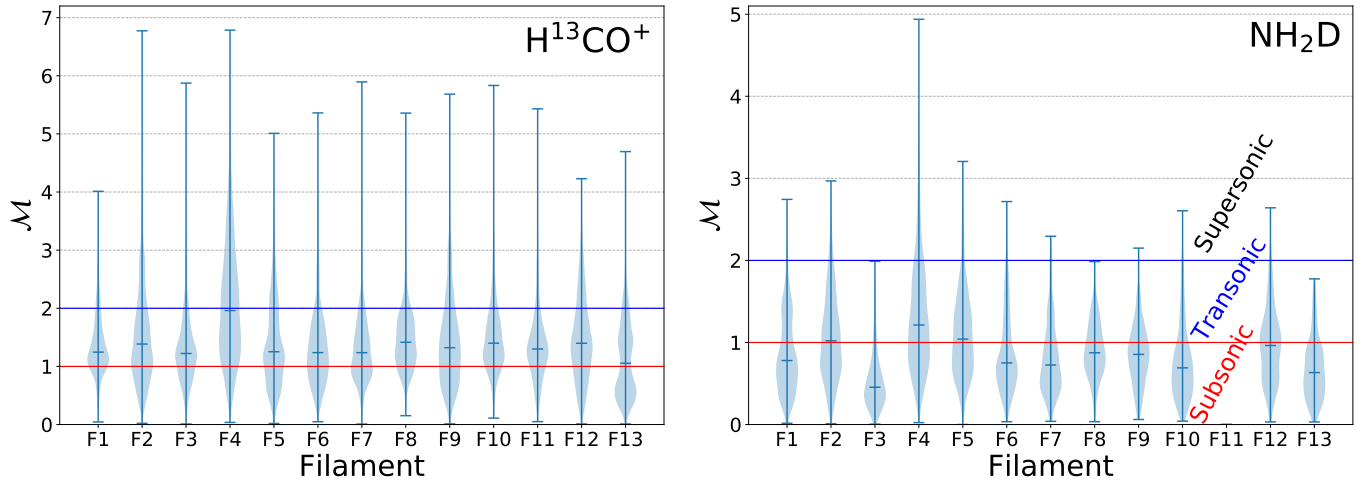


**Figure 7.** Left and right: violin plots of the Mach number distributions derived from  $\text{H}^{13}\text{CO}^+$  and  $\text{NH}_2\text{D}$  for each filament. The blue bars from the top to the bottom represent the maximum, mean, and minimum values, respectively. The red and blue solid lines are the Mach number of 1 and 2, respectively.

497 from the trigonometric parallax measurement is  $\sim 20\%$   
 498 (Chibueze et al. 2014). The standard deviation (std) of  
 499  $X(\text{H}^{13}\text{CO}^+)$  for F4 is about  $3.7 \times 10^{-11}$ , which corre-  
 500 sponds to  $1\sigma$  uncertainty of  $70\% = \frac{3.7 \times 10^{-11}}{5.4 \times 10^{-11}}$ . We settle  
 501 on an uncertainty estimate of a factor of  $\sim 2$  for both fil-  
 502 ament mass and mass per unit length according to the  
 503 propagation of error. Considering of the inclination an-  
 504 gle is unknown, the uncertainties in the mass per unit  
 505 length could be larger.

### 506 3.6. Subsonic and Transonic Filaments

507 The three-dimensional (3D) Mach number is  $\mathcal{M} =$   
 508  $\sqrt{3}\sigma_{\text{nth}}/c_s$ , where  $\sigma_{\text{nth}} = \sqrt{\sigma_{\text{obs}}^2 - (\Delta_{\text{ch}}/2\sqrt{2\ln 2})^2} - \sigma_{\text{th}}^2$   
 509 is the nonthermal velocity dispersion,  $c_s$  is the sound  
 510 speed, and  $\Delta_{\text{ch}}$  is the channel width. The molecular  
 511 thermal velocity dispersion can be estimated by  $\sigma_{\text{th}} =$   
 512  $\sqrt{(k_B T)/(\mu m_H)} = 0.098 \text{ km s}^{-1} (\frac{T}{\text{K}})^{0.5} \mu^{-0.5}$ , where  $\mu =$   
 513  $m/m_H$  is the molecular weight,  $m$  is the molecular mass,  
 514  $m_H$  is the hydrogen mass, and  $T$  is the gas temperature  
 515 (see also Paper I). The sound speed  $c_s$  was estimated us-  
 516 ing a mean molecular weight per free particle of  $\mu_p = 2.37$   
 517 (Kauffmann et al. 2008). Figure 7 shows the Mach num-  
 518 ber ( $\mathcal{M}$ ) distributions derived from  $\text{H}^{13}\text{CO}^+$  and  $\text{NH}_2\text{D}$   
 519 for each filament, except for F11 which has no significant  
 520  $\text{NH}_2\text{D}$  detection. Some filaments are partially overlap-  
 521 ping but the corresponding  $\text{NH}_2\text{D}$  line emission shows  
 522 only one velocity component clearly. This  $\text{NH}_2\text{D}$  emis-  
 523 sion is assigned to a particular filament based on the  
 524 minimum velocity differences between  $\text{NH}_2\text{D}$  emission  
 525 and that filament. The Mach number distributions deriv-  
 526 ed from both  $\text{H}^{13}\text{CO}^+$  and  $\text{NH}_2\text{D}$  lines reveal that  
 527 the majority of filaments are subsonic ( $\mathcal{M} \leq 1$ ) and  
 528 transonic ( $1 < \mathcal{M} \leq 2$ ) in nonthermal motions. In gen-  
 529 eral, the  $\mathcal{M}$  derived from  $\text{NH}_2\text{D}$  tends to be smaller

530 than those from  $\text{H}^{13}\text{CO}^+$ . This is because  $\text{NH}_2\text{D}$  emis-  
 531 sion traces colder, denser gas and it is less affected by  
 532 the protostellar feedback (e.g., outflows) as compared to  
 533 the  $\text{H}^{13}\text{CO}^+$  emission; this is confirmed by the fact that  
 534 the observed line widths of the former narrower than  
 535 those of the latter. The subsonic and transonic features  
 536 imply a quiescent nature of these filaments. The sub-  
 537 sonic and transonic nonthermal line widths found here  
 538 in dense filaments and dense cores have been seen pre-  
 539 viously in low-mass star-forming regions (e.g., Perseus,  
 540 Pineda et al. 2010; Serpens, Gong et al. 2021; Ophiuchus  
 541 and Taurus, Chen et al. 2019a; L1478 in the California,  
 542 Chung et al. 2019), intermediate- and high-mass star-  
 543 forming regions (e.g., Orion, Hacar et al. 2018; Mon-  
 544 sch et al. 2018; Yue et al. 2021; IRDC G035.39-00.33,  
 545 Sokolov et al. 2018; IRDC G14.225-0.506, Chen et al.  
 546 2019b).

## 547 4. DISCUSSION

### 548 4.1. Continuum Filament

549 The majority of the continuum emission structures  
 550 have a significant line emission counterparts. One ex-  
 551 ception is the continuum filamentary structure in the  
 552 south-eastern part of the map (see Figures 1 and 2),  
 553 which has no line emission counterpart except for a small  
 554 area near the middle that shows weak emission in the  
 555  $\text{H}^{13}\text{CO}^+$ , CS, HCN and  $\text{HCO}^+$  lines. If this filamentary  
 556 structure's continuum emission was dominated by free-  
 557 free or synchrotron emission rather than dust emission,  
 558 the stellar feedback from O type stars (O7.5 and O6.5,  
 559 see Figure 1; Persi & Tapia 2008) on the north-eastern  
 560 side of NGC 6334S are most likely responsible.

561 We used the `FilFinder` to extract this filamentary  
 562 structure and its filament spine (see Figure 8). The fil-

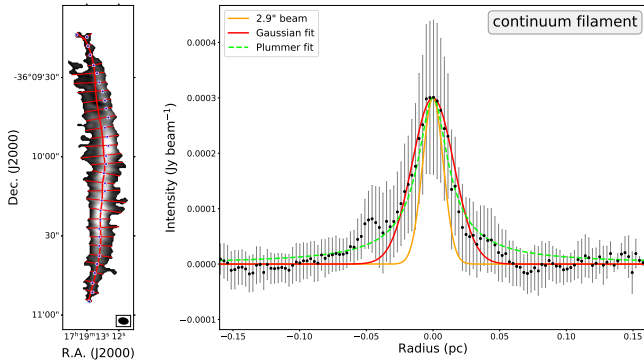


**Figure 8.** Left: the filament spine (red solid curve) of continuum filament overlaid on the 3 mm continuum image. Right: mean integrated intensity profile (black dots) was built by sampling radial cuts (short red solid lines) every 8 pixels ( $3''.44$  corresponds to  $\sim 0.019$  pc at the source distance of 1.3 kpc) along the spine. The radial distance is the projected distance from the peak emission at a given cut (blue dots in the left panel). The error bar represents the standard deviation of the cuts at each radial distance. The orange solid line shows the beam response with a FWHM of  $\sim 2.9''$ . The red solid and green dashed lines present the best-fit results of Gaussian and Plummer fitting, respectively.

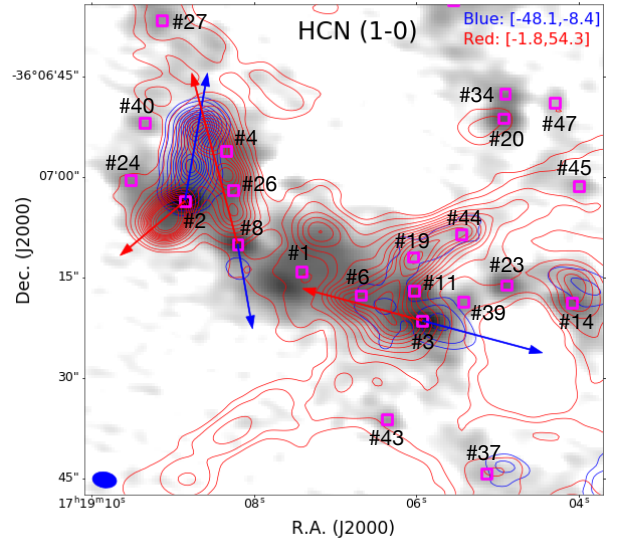


**Figure 9.** Magenta open squares show the continuum cores. The blue-shifted (blue contours) and red-shifted (red contours) of HCN (1-0) line emission overlaid on the continuum image. The arrows show the outflow directions. The beam size is shown in the bottom left of each panel.

563 ament length is about 0.8 pc. Using *Radfil*, the fila-  
 564 ment widths are about 0.032 pc and 0.023 pc derived by  
 565 Gaussian and Plummer fitting based on the continuum  
 566 emission (Table 1), respectively. The gas mass cannot  
 567 be reliably estimated because of the unknown fraction  
 568 of dust emission.

#### 4.2. The Kinematics of Filaments

570 Figure 6 shows the variations of  $v_{\text{LSR}}$  and  $\sigma_{\text{obs}}$  derived  
 571 from the  $\text{H}^{13}\text{CO}^+$  line emission along the filament. Only  
 572 one filament (F1) shows monotonic changes along the fil-  
 573 ament in  $v_{\text{LSR}}$ . In contrast, the  $\sigma_{\text{obs}}$  shows small fluctu-  
 574 ations along F1 rather than monotonic change. Four  
 575 continuum cores and two  $\text{NH}_2\text{D}$  cores are associated  
 576 with this filament. The core mean  $\sigma_{\text{obs}}$  derived from the  
 577  $\text{H}^{13}\text{CO}^+$  line is comparable to the  $\sigma_{\text{obs}}$  of filament, how-  
 578 ever continuum cores #25 and #21 have slightly larger  
 579  $\sigma_{\text{obs}}$ . Line widths may be broadened by active star for-  
 580 mation. In contrast, some cores show much narrower  
 581  $\sigma_{\text{obs}}$  than their respective filament; e.g., #31/#36/#49  
 582 in F2, #4/#24 in F4, M11 in F5, M10 in F6, M14 in  
 583 F10. The measured  $\sigma_{\text{obs}}$  of  $\text{NH}_2\text{D}$  is always narrower  
 584 than those of  $\text{H}^{13}\text{CO}^+$  toward the continuum cores and  
 585  $\text{NH}_2\text{D}$  cores, and this feature is also seen in the fila-  
 586 ments (see Figure 7). In Section 4.4, we will discuss the  
 587 properties of  $\sigma_{\text{obs}}$  in both continuum cores and  $\text{NH}_2\text{D}$   
 588 cores.

589 Some filaments show only small  $v_{\text{LSR}}$  variations along  
 590 their spine (F4b, F5, F7, F8, F10, F10b, F12), while

591 others display significant variations (F2, F3, F4, F6,  
 592 F9, F11, F13). The  $\sigma_{\text{obs}}$  also shows irregular varia-  
 593 tions in all of filaments, except for F1 and F13. The  
 594 latter shows roughly an increasing trend from east to  
 595 west (Figure 13). There is another gaseous structure  
 596 seen in the CS (1-0),  $\text{HCO}^+$  (1-0), and HCN (1-0) lines,  
 597 which runs northwest to southeast through the western  
 598 part of F13. The interaction between two gas flows can  
 599 broaden the  $\text{H}^{13}\text{CO}^+$  line widths around the intersection  
 600 regions. On the other hand, the star formation activity  
 601 is responsible for some of the  $v_{\text{LSR}}$  and  $\sigma_{\text{obs}}$  varia-  
 602 tions in some filaments. For instance, F4 shows  $v_{\text{LSR}}$  and  $\sigma_{\text{obs}}$   
 603 variations at positions in which several strong molecular  
 604 outflows are detected in the HCN,  $\text{HCO}^+$ , and CS lines  
 605 (see Figure 9). These molecular outflows can inject en-  
 606 ergy and momentum into the immediate surroundings  
 607 of protostars and affect the gas kinematics, and then  
 608 the turbulence (or line width) will be increased and the  
 609 gas velocity will be modified (Li et al. 2019b, 2020b; Lu  
 610 et al. 2021). Filament F4 encompasses the highest num-  
 611 ber of continuum cores and YSOs among the filaments  
 612 (Figures 1 and 13), and therefore the  $v_{\text{LSR}}$  and  $\sigma_{\text{obs}}$  of  
 613 the  $\text{H}^{13}\text{CO}^+$  line emission in F4 is most likely signifi-  
 614 cantly affected by protostellar feedback. Overall, both  
 615 protostellar activity and interaction between gas flows  
 616 can significantly alter the local gas kinematics.

#### 4.3. Velocity Gradient Along F1

618 As shown in Figure 6, F1 presents a smooth veloc-  
 619 ity change in  $\text{H}^{13}\text{CO}^+$  emission from the south ( $-3.3$  km

s<sup>-1</sup>) to the north (-1.8 km s<sup>-1</sup>) along the filament, resulting in a projected velocity gradient of  $\sim 1.8 \pm 0.1$  km s<sup>-1</sup> pc<sup>-1</sup>. The NH<sub>2</sub>D line emission also shows a similar velocity gradient along F1. The velocity gradient along F1 could be attributed to the ongoing accretion flow in F1 (e.g., Kirk et al. 2013), whereas we cannot completely rule out the possibility that the gas kinematics is affected by the external feedback from the western YSOs, such as molecular outflows and/or expanding shells.

If the velocity gradient comes from the accretion flow along the F1 filament, one can estimate the mass flow rate using the derived velocity gradient and filament mass. Assuming that the filament has a cylindrical geometry, the mass flow rate,  $\dot{M}$ , can be calculated as (see Kirk et al. 2013)

$$\dot{M} = \frac{M \nabla_{\parallel} v_{\text{obs}}}{\tan(\alpha)} \quad (4)$$

where  $M$  is the filament mass,  $\nabla_{\parallel} v_{\text{obs}}$  is the observed velocity gradient along the filament, and  $\alpha$  is the angle of inclination to the plane of sky. Using the derived filament mass of 14 M<sub>⊙</sub>, the observed velocity gradient of 1.8 km s<sup>-1</sup> pc<sup>-1</sup>, and assuming a moderate inclination angle of  $\alpha = 45^\circ$ , the mass flow rate is estimated to be about 26 M<sub>⊙</sub> Myr<sup>-1</sup> for F1. This result indicates that the F1 filament will double its mass in several free-fall time;  $\sim 1 \times 10^5$  yrs assuming a density of 10<sup>5-6</sup> cm<sup>-3</sup> that is the typical value of continuum cores in the F1 (see Paper I).

Considering the uncertainties of the derived mass and inclination angle, the estimated flow accretion is roughly comparable to the values of 70 ± 40 M<sub>⊙</sub> Myr<sup>-1</sup> in the IRDC G035.39-00.33 (Henshaw et al. 2014), and 17 – 72 M<sub>⊙</sub> Myr<sup>-1</sup> in the Monoceros R2 (Treviño-Morales et al. 2019), and 20 – 130 M<sub>⊙</sub> Myr<sup>-1</sup> in the IRDC G14.225-0.506 (Chen et al. 2019b). The estimated mass flow rate could be treated as a lower limit, because the H<sup>13</sup>CO<sup>+</sup> only traces relatively high dense gas and F1 filament is only a small part of a much large filamentary structure seen in the infrared image (see Figure 1).

A velocity gradient is also detected in sections of the other filaments (e.g., F7 and F13) and around some embedded cores (e.g., #29 in the F3; see Figure 13). Unfortunately, in these cases we cannot distinguish whether the velocity gradient is the result of gas flow or some other physical process, e.g., molecular outflow or rotation. Thus, we refrain from estimating the mass flow rate for other filaments.

#### 4.4. The Kinematics of Embedded Cores

As mentioned in Section 4.3, some cores show smaller  $\sigma_{\text{obs}}$  compared to their immediate surrounding. This is

probably because the surrounding gas is affected by the protostellar activity (e.g., molecular outflows) for some cores. For instance, there is a molecular outflow emanating from #2 in the immediate vicinity of cores #4 and #24, thus the H<sup>13</sup>CO<sup>+</sup> line widths around both #4 and #24 can be broadened by this outflow activity (see Figure 2). The outflow driven by core #8 also affects the molecular gas around the core #4. The details of molecular outflow analysis is beyond the scope of this paper but is the topic of a followup paper.

Furthermore, some of the cores indeed have narrow line widths as revealed by the NH<sub>2</sub>D line, which is less affected by the molecular outflows than H<sup>13</sup>CO<sup>+</sup> as mentioned above. In addition, there are no outflow signatures around these cores. For instance, the observed velocity dispersion appears to decrease toward the center of M1 (See Figure 10). A trend of  $\sigma_{\text{obs}}$  decreasing with decreasing radial distance ( $R_{\text{dist}}$ ) from the center of core is found in 16 cores (see Figure 10), including 6 continuum cores (#5, #10, #22, #25, #35, and #37) and 10 NH<sub>2</sub>D cores (M1, M4, M6, M7, M8, M9, M13, M10, M15, and M17; see also Figure 3 in Paper II for M1). Note that the annularly averaged  $\sigma_{\text{obs}}$  has relatively large uncertainties toward the outer edges of the cores due to the low S/N. The decreasing trend of  $\sigma_{\text{obs}}$  toward these core centres may indicate that turbulent dissipation from the filaments to the embedded objects is ongoing, enabling the dense precursors to collapse to form protostars. Alternatively, a number of theoretical studies suggest that for pre-stellar cores the line width will be smaller in the more central regions if the infall speed decreases toward the center because of an outside-in collapse (e.g., Whitworth & Summers 1985; Lai 2000; Gómez et al. 2021). In summary, some dense cores indeed have narrower observed velocity dispersion compared to their natal filaments. This may indicate that turbulent dissipation is taking place in these embedded cores.

#### 4.5. Filament Stability

The comparison between the  $M_{\text{line}}$  and the corresponding critical line-mass  $M_{\text{crit}} = 2\sigma_{\text{eff}}^2/G$  can be used to evaluate the stability of the filament; where  $\sigma_{\text{eff}}$  is the effective velocity dispersion and  $G$  is the gravitational constant (see Appendix B for the estimation of critical line-mass.). Ignoring external pressure and magnetic fields, we computed the  $M_{\text{crit}}$  for thermally supported ( $\sigma_{\text{eff}} = c_s$ ), nonthermal motions supported ( $\sigma_{\text{eff}} = \sigma_{\text{nth}}$ ), and total motions supported (i.e. including both thermal and nonthermal contributions,  $\sigma_{\text{eff}} = \sqrt{c_s^2 + \sigma_{\text{nth}}^2}$ ) filaments. As shown in Figure 11,  $M_{\text{line}}$  is larger than the thermal critical mass ( $M_{\text{crit,th}}$ ), except for F4b, F6



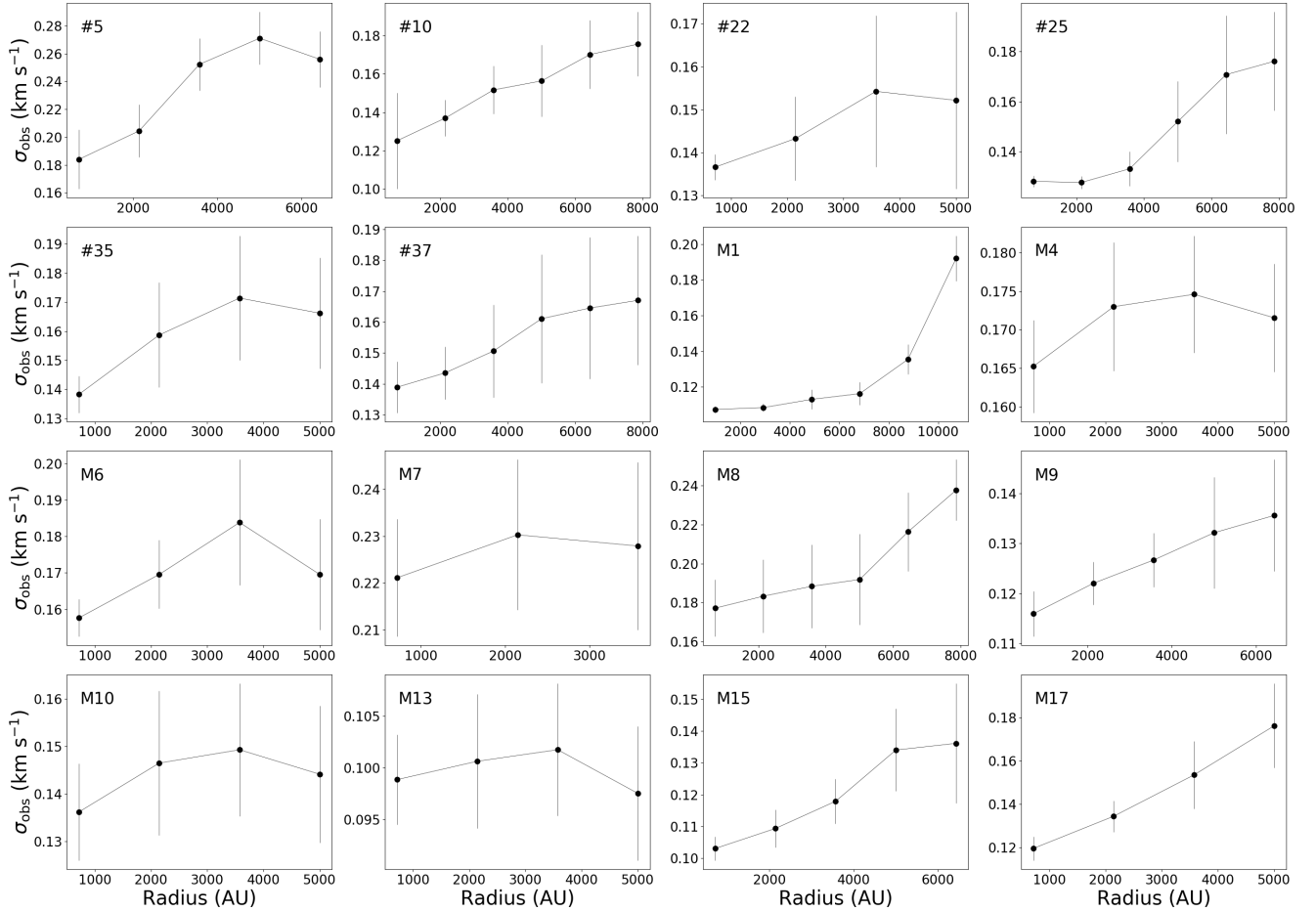


**Figure 10.** The annularly averaged observed  $\text{NH}_2\text{D}$  velocity dispersions ( $\sigma_{\text{obs}}$ ) as a function of radial distance from the center of cores. The error bars show the statistical standard deviation inside each ring divided by the square root of the length of the ring. M1 is modified from Paper II. The name of each core is shown in the top left of each panel.

713 and F13 that are smaller than the  $M_{\text{crit,th}}$ . This indicates that the filaments would be gravitationally bound (except for F4b, F6 and F13) in the purely thermally supported case.  $M_{\text{line}}$  is about 2 times the nonthermal critical mass ( $M_{\text{crit,nth}}$ ), which suggests that nonthermal support alone cannot prevent gravitational collapse. The ratios of  $M_{\text{crit,nth}}/M_{\text{crit,th}}$  are in the range 0.4–1.4 with a mean value of 0.7, which suggests that the filaments are mostly supported by thermal motions. The estimated  $M_{\text{line}}$  is smaller than the total critical ( $M_{\text{crit,tot}}$ ) mass in all the filaments, except for F4.

724 Although most of the filaments at the current evolutionary state are gravitationally unbound when considering only the balance between self-gravity and the thermal plus nonthermal support, the presence of dense cores suggests that in fact star formation has already started. Note that by neglecting external pressure, magnetic field, mass uncertainty, and inclination angle uncertainty might bring an addition error into the  $M_{\text{line}}/M_{\text{crit,tot}}$ . Being gravitationally bound is not the

733 sole prerequisite for forming stars in a filament. The fragmentation may have occurred already very early in the evolution of the filaments, if these dense cores originate from filament fragmentation. In addition, the subsonic and transonic dominated filaments and embedded cores indicate that there are low turbulence environments (Paper II); this is analogous to the situation in low-mass star-forming clouds (e.g., Hartmann 2002; Pineda et al. 2010; Hacar & Tafalla 2011; Hacar et al. 2016, 2017). The similarity suggests that similar turbulent conditions may apply in the very early evolutionary phases of low- and high-mass star formation at clump scales ( $\leq$  of a few pc) where turbulence inherited from larger scales (e.g., giant molecular clouds) has already decayed or dissipated in a short timeframe (Mac Low 1999; Mac Low & Klessen 2004).

749 Figure 11 shows  $M_{\text{line}}$  as a function of  $\sigma_{\text{nth}}/c_s$ . The derived masses per unit length are similar to those of narrow filaments in B213-L1495 ( $24 \pm 19 M_{\odot} \text{ pc}^{-1}$ ), Musca ( $26 M_{\odot} \text{ pc}^{-1}$ ), NGC 1333 ( $34 \pm 22 M_{\odot} \text{ pc}^{-1}$ ), and Orion

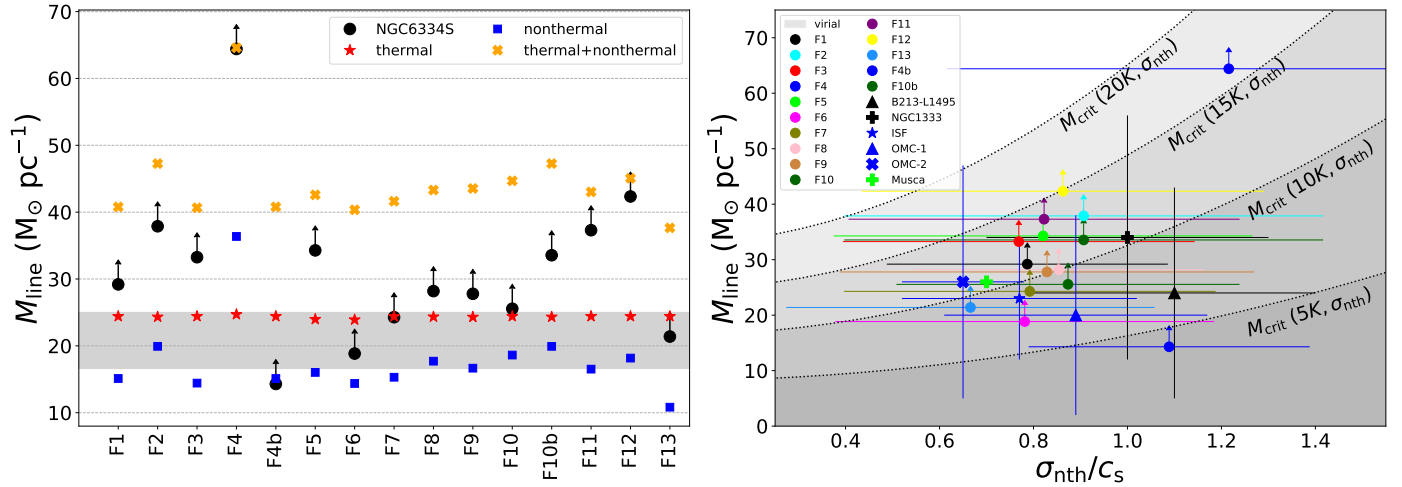


**Figure 11.** Left: the line-mass for each filament. The black filled circles, red filled stars, blue filled squares, and orange filled crosses show the estimated mass per unit length, thermal critical line-mass, nonthermal critical line-mass, and total (thermal + nonthermal) critical line-mass, respectively. The shaded gray region shows the thermal critical line-mass of  $16.6 - 25 M_{\odot} \text{pc}^{-1}$  corresponding to the gas temperature of  $10 - 15 \text{ K}$ . The arrows indicate that the estimated mass per unit length could be treated as a lower limit. Right: mass per unit length vs.  $\sigma_{\text{nth}}/c_s$ . The error bars indicate the standard deviation of the parameters. The dashed lines show the expected total critical line-mass for an infinite filament in hydrostatic equilibrium at temperatures of  $5 \text{ K}$ ,  $10 \text{ K}$ ,  $15 \text{ K}$ , and  $20 \text{ K}$ , respectively (see Appendix B). The data points of B213-L1495, NGC1333, ISF, OMC1, OMC2, and Musca are retrieved from Hacar et al. (2018).

( $23 \pm 11 M_{\odot} \text{pc}^{-1}$  for ISF,  $20 \pm 18 M_{\odot} \text{pc}^{-1}$  for OMC-1, and  $26 \pm 21 M_{\odot} \text{pc}^{-1}$  for OMC-2; Hacar et al. 2013, 2016, 2017, 2018). The measured  $\sigma_{\text{nth}}/c_s$  are also comparable to those narrow filaments in the B213-L1495, Musca, NGC 1333, and Orion (OMC-1/2 and ISF; see Figure 11). These results indicate that the masses per unit length and gas kinematics of narrow filaments in NGC 6334S are comparable to those found in various other environments, from low-mass to high-mass star-forming molecular clouds.

The total gas mass computed from  $\text{H}^{13}\text{CO}^+$  is about  $395 M_{\odot}$ , which is larger than the total gas mass of  $160 M_{\odot}$  estimated from continuum emission. The  $\text{H}^{13}\text{CO}^+$  recovers about 28% of the accumulated mass ( $1389 M_{\odot}$ ) derived from  $\text{H}_2$  column density map (derived in Paper I; see Appendix A in Paper I for detailed derivation of  $\text{H}_2$  column density.) This indicates that the extended flux, which contains a significant amount of mass, is not fully recovered by the  $\text{H}^{13}\text{CO}^+$  line toward NGC 6334S in this ALMA observation. The estimated filament masses should thus be treated as lower limits because  $\text{H}^{13}\text{CO}^+$  ( $1-0$ ;  $n_{\text{cr}} \sim 10^5 \text{ cm}^{-3}$ ) only probes higher density gas components; moreover, the data suffer from missing flux due to the lack of short spacing observations.

#### 4.6. Population of Embedded Cores and YSOs

The continuum cores are likely at protostellar or pre-stellar evolutionary phases, while the  $\text{NH}_2\text{D}$  cores seem at the starless/pre-stellar phases (see Paper II). Fig-

ure 1(b) shows the distribution of identified dense objects and filaments toward NGC 6334S. The majority of the 45 continuum cores are associated with filaments, while only 4 continuum cores (#22, #28, #33 and #48) are not associated with any identified filament. In addition, 15 out of 17  $\text{NH}_2\text{D}$  cores are associated with filaments. These results indicate that the majority of dense cores are closely related with filaments in NGC 6334S; as noted earlier, this situation is also found in nearby low-mass star-forming regions (e.g., André et al. 2010).

Figure 1(b) also shows the YSOs spatial distributions toward NGC 6334S. There are 25 Class I and 58 Class II YSOs in the NGC 6334S. The Class I and II YSOs are identified with the near-IR (NEWFIRM) and mid-IR (IRAC) data (see Willis et al. 2013). Among the 49 identified continuum cores, 12 cores are spatially associated with Class I objects, 5 cores are spatially associated with Class II objects, and the remaining 32 cores do not have YSOs counterparts. This indicates that these 32 cores could be younger compared to those cores associated with Class I and Class II YSOs. The majority of YSOs have no continuum core counterparts, perhaps because their continuum emission is too faint ( $1\sigma \sim 0.03 \text{ mJy beam}^{-1}$ , or  $\sim 0.04 M_{\odot}$  at a temperature of  $10 \text{ K}$ ). Furthermore, the YSOs are not associated with  $\text{NH}_2\text{D}$  cores counterparts, because the  $\text{NH}_2\text{D}$  line emission is in cold dense gas still in its extremely early evolutionary stages (e.g., starless and/or pre-stellar).

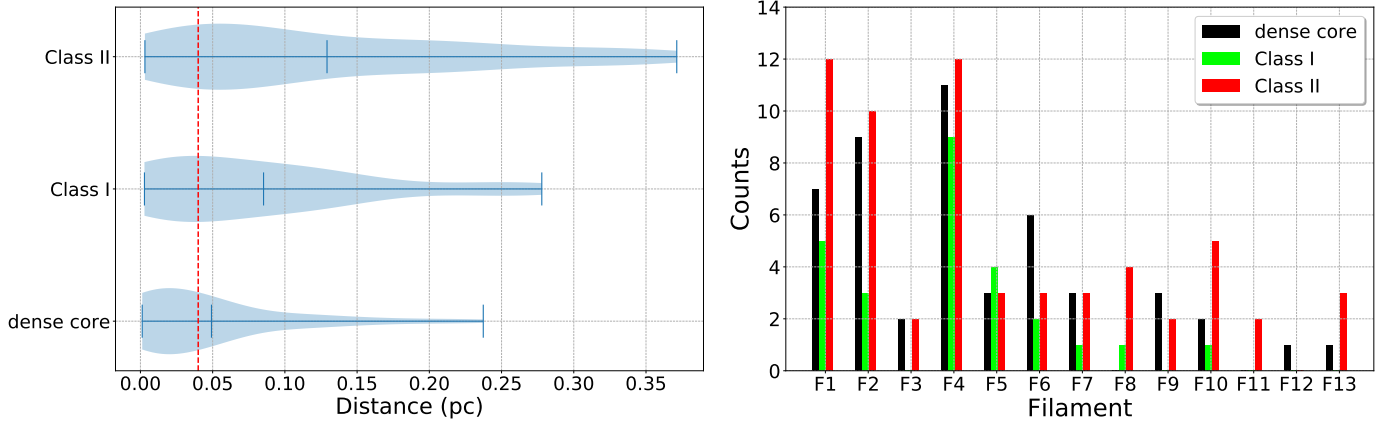


**Figure 12.** Left: violin plot of the distance distributions for each type object, where the distances are the objects to the nearest filament spine. The shape of each distribution shows the probability density of the data smoothed by a kernel density estimator. The blue bars from the top to bottom represent the maximum, mean, and minimum values, respectively. The vertical red dashed line is the mean beam-convolved filament width of  $\sim 0.04$  pc. Right: the number of the nearest dense cores, Class I and Class II objects for each filament.

810 The majority of continuum cores,  $\text{NH}_2\text{D}$  cores, and  
 811 Class I objects reside in or close to a filament, while the  
 812 majority of Class II objects are far away (see Figures 1  
 813 and 2). We computed the distance of these objects to  
 814 their nearest filament spine, in order to search for possi-  
 815 ble correlations between the evolutionary stages and the  
 816 distance from the filament. Based on the distance dis-  
 817 tribution of each type of object shown in Figure 12(a),  
 818 Class II objects have larger distances than Class I, while  
 819 Class I objects have larger distance than the distribu-  
 820 tion of continuum cores and  $\text{NH}_2\text{D}$  cores. Continuum  
 821 cores and  $\text{NH}_2\text{D}$  cores are classified as the same type  
 822 of object in this analysis because the majority of them  
 823 are embedded in filaments and their evolutionary stages  
 824 (pre-stellar or protostellar) are earlier than Class I/II  
 825 (Paper II). The median distances are 0.09 pc, 0.06 pc,  
 826 and 0.03 pc for Class II, Class I, and dense cores, re-  
 827 spectively. Overall, Figure 12(a) indicates that the more  
 828 evolved objects are further away from the dense gas fil-  
 829 aments in NGC 6334S.

830 One possible explanation for the different distance dis-  
 831 tributions is that the evolved objects are moving away  
 832 from their parental dense filament due to the kinemat-  
 833 ical motions (e.g., slingshot mechanism and ejection;  
 834 Stutz & Gould 2016; Russeil et al. 2020). Assuming  
 835 the Class II are moving  $1 \text{ km s}^{-1}$  relative to the fila-  
 836 ments (the typical moving velocity of Class II in Orion;  
 837 Stutz & Gould 2016), the estimated moving timescales  
 838 are between  $3 \times 10^3$  and  $4 \times 10^5$  yr, with a median value  
 839 of  $9 \times 10^4$  yr. We would like to stress the fact that the  
 840 actual moving distances may be much smaller than the  
 841 estimated distances because the YSOs might not neces-  
 842 sarily form in the centre of the filament. Therefore, the  
 843 actual dynamical timescales could be smaller than the

844 estimated values. Another possibility is that NGC 6334S  
 845 has experienced star formation before, and the parental  
 846 molecular structures of Class II have already been moved  
 847 away from the YSOs (e.g., Vázquez-Semadeni et al.  
 848 2017; Kumar et al. 2020) or dispersed/destroyed by star  
 849 formation feedback. Finally, we cannot rule out the pos-  
 850 sibility that a few Class II objects may have originated  
 851 outside of NGC 6334S; especially those objects that are  
 852 distant from the filaments.

853 The number of nearest dense cores, Class I, and  
 854 Class II for each filament is presented in Figure 12(b).  
 855 The number of dense cores and Class I around F4 is  
 856 much higher than for the rest of filaments, while the  
 857 number of Class II around F1, F2, and F4 is compa-  
 858 rable and higher than in the other filaments. F4 is lo-  
 859 cated at the central region where encompasses a signif-  
 860 icant fraction of dense gas and thus it has potential to  
 861 form more stars as evidenced by the numerous contin-  
 862 uum cores and YSOs. F2 has the longest physical length  
 863 in NGC 6334S, and thus, it is expected to be associated  
 864 with more YSOs. As shown in Figure 1, a cluster of  
 865 YSOs is forming on the western side of F1, resulting in  
 866 a large number of nearest YSOs. We note that F1 is  
 867 only a small part of a much larger filamentary structure  
 868 seen in the infrared image (see Figure 1), implying that  
 869 it has a large dense gas reservoir from which to form  
 870 more stars.

871 In summary, all identified filaments show a narrow  
 872 width and the majority of them host embedded dense  
 873 core. These embedded dense cores are born in environ-  
 874 ments of low turbulence, which is similar to conditions  
 875 found in low-mass star-forming regions. More evolved  
 876 objects are found to be farther away from the filaments,



877 suggesting YSOs or filaments have a tendency to move  
878 away from their natal place as they evolve.

## 879 5. CONCLUSION

880 In this paper, we investigated the velocity-coherent filaments in the massive IRDC NGC 6334S using ALMA  
881 observations. Using the  $\text{H}^{13}\text{CO}^+$  (1-0) line emission, we  
882 have identified 13 velocity-coherent filaments. We investigated the physical properties of the identified filaments  
883 and characterized the dense objects in the NGC 6334S.  
884 Our main findings are summarized as follows:  
885

- 887 1. The filaments show a compact radial distribution  
888 with a median  $\text{FWHM}_{\text{decon}}$  of  $\sim 0.04$  pc. The  
889 derived filament widths are narrower than the  
890 previously proposed ‘quasi-universal’ 0.1 pc filament  
891 width. In addition, the filament widths are  
892 roughly twice the size of embedded cores (radius  
893  $\sim 0.017$  pc). The higher spatial resolution observations  
894 and higher-density gas tracer tend to identify  
895 even narrower and lower mass filaments.
- 896 2. The nonthermal motions are predominantly subsonic  
897 and transonic in all observed filaments; the  
898 single exception is F4 which has been significantly  
899 affected by protostellar feedback. The filaments  
900 are largely supported by thermal motions. The  
901 physical properties (mass, mass per unit length,  
902 gas kinematics, and width) of filaments are similar  
903 to those seen in narrow filaments found in various  
904 other kinds of environments such as low-mass,  
905 intermediate-mass, and high-mass star-forming regions  
906 (i.e., B213-L1495, Musca, NGC 1333, Orion,  
907 and G035.39-00.33).
- 908 3. A fraction of the embedded objects show narrower  
909 observed velocity dispersions ( $\sigma_{\text{obs}}$ ) than  
910 their natal filaments, which may indicate that  
911 turbulent dissipation is taking place in these  
912 embedded cores. The subsonic and transonic dominated  
913 filaments and dense cores indicate that in  
914 NGC 6334S the stars are often born in environments  
915 of low turbulent motions. This conclusion hints  
916 that similar small turbulent conditions exist at  
917 very early evolutionary stages of low- and  
918 high-mass star formation at clump scales.
- 919 4. The median distance to the nearest filament for  
920 dense cores, Class I, and Class II, is 0.03 pc,  
921 0.06 pc, and 0.09 pc respectively. The increasing  
922 distances suggest that the more evolved objects  
923 are farther away from the filaments in the  
924 NGC 6334S, perhaps because either YSOs or  
925 filaments tend to move away from their natal place  
926 as they evolve.

## ACKNOWLEDGMENTS

We thank the anonymous referee for the constructive report. D.L. acknowledges the support from the National Natural Science Foundation of China grant No. 11988101. C.W.L. is supported by the Basic Science Research Program through the National Research Foundation of Korea (NRF) funded by the Ministry of Education, Science and Technology (NRF-2019R1A2C1010851). P.S. was partially supported by a Grant-in-Aid for Scientific Research (KAKENHI Number 18H01259) of the Japan Society for the Promotion of Science (JSPS). H.B. acknowledges support from the Deutsche Forschungsgemeinschaft (DFG, German Research Foundation) – Project-ID 138713538 – SFB 881 (“The Milky Way System”, subproject B1). H.B. further acknowledges funding from the European Research Council under the Horizon 2020 Framework Program via the ERC Consolidator Grant CSF-648505. J.M.G. acknowledges the support of the grants AYA2017-84390-C2-R and PID2020-117710GB-I00 (AEI/FEDER, UE). A.P. acknowledges financial support from the UNAM-PAPIIT IN111421 grant, the Sistema Nacional de Investigadores of CONACyT, and from the CONACyT project number 86372 of the ‘Ciencia de Frontera 2019’ program, entitled ‘Citlalcóatl: Amultiscale study at the new frontier of the formation and early evolution of stars and planetary systems’, México. I.J.-S. has received partial support from the Spanish State Research Agency (AEI) project number PID2019-105552RB-C41. This paper makes use of the following ALMA data: ADS/JAO.ALMA#2016.1.00951.S. ALMA is a partnership of ESO (representing its member states), NSF(USA) and NINS (Japan), together with NRC (Canada) and NSC and ASIAA (Taiwan) and KASI (Republic of Korea), in cooperation with the Republic of Chile. The Joint ALMA Observatory is operated by ESO, AUI/NRAO and NAOJ.

927 *Facilities:* ALMA, Herschel.

928 *Software:* CASA (McMullin et al. 2007), APLpy  
929 (Robitaille & Bressert 2012), Matplotlib (Hunter 2007),  
930 Astropy (Astropy Collaboration et al. 2013), PySpecKit  
931 (Ginsburg & Mirocha 2011), Numpy (Harris et al. 2020).

Table 1. Physical parameters of the filaments.

Filament	Gaussian										Plummer				
	$L_{\text{fil}}$	$M_{\text{fil}}$	$M_{\text{line}}$	$M_{\text{crit,tot}}$	$M_{\text{crit,nth}}$	$M_{\text{crit,th}}$	$A_0$	stddev	FWHM	FWHM <sub>decon</sub>	$A_0$	$R_{\text{flat}}$	$p$	FWHM	FWHM <sub>decon</sub>
(1)	(2)	(3)	(4)	(5)	(6)	(7)	(8)	(9)	(10)	(11)	(12)	(13)	(14)	(15)	(16)
	(pc)	( $M_{\odot}$ )	( $M_{\odot} \text{ pc}^{-1}$ )	( $M_{\odot} \text{ pc}^{-1}$ )	( $M_{\odot} \text{ pc}^{-1}$ )	( $M_{\odot} \text{ pc}^{-1}$ )	( $10^{-2} \text{ Jy/beam km/s}$ )	(pc)	(pc)	(pc)	( $10^{-2} \text{ Jy/beam km/s}$ )	(pc)		(pc)	(pc)
F1	0.48	14	29	41	15	24	8.45±0.12	0.020	0.047	0.042	8.53±0.12	0.057±0.009	9.78±2.37	0.047	0.042
F2	1.37	52	38	47	20	24	5.20±0.06	0.026	0.061	0.057	5.16±0.14	0.081±0.030	10.05±5.74	0.066	0.062
F3	0.50	17	33	41	14	24	7.30±0.11	0.023	0.054	0.049	7.25±0.20	0.051±0.012	6.27±1.99	0.056	0.051
F4	1.27	82	64	65	36	25	8.39±0.23	0.021	0.049	0.044	8.84±0.26	0.021±0.004	2.81±0.34	0.045	0.039
F4b	0.27	4	14	41	15	24	9.90±0.21	0.019	0.045	0.040	10.05±0.29	0.014±0.003	1.84±0.17	0.057	0.053
F5	0.53	18	34	41	16	24	6.37±0.16	0.024	0.056	0.052	6.73±0.22	0.024±0.004	2.78±0.30	0.051	0.047
F6	0.86	16	19	43	14	24	5.06±0.11	0.015	0.036	0.029	5.16±0.15	0.023±0.006	3.94±1.08	0.036	0.029
F7	0.62	15	24	40	15	24	3.65±0.18	0.016	0.037	0.030	3.77±0.22	0.015±0.006	2.40±0.55	0.038	0.032
F8	0.40	11	28	42	18	24	7.46±0.22	0.015	0.036	0.029	7.62±0.19	0.034±0.007	7.16±2.05	0.034	0.027
F9	0.82	23	28	43	17	24	3.92±0.13	0.031	0.074	0.071	4.29±0.15	0.021±0.005	2.17±0.24	0.064	0.060
F10	0.53	13	26	44	19	24	8.34±0.23	0.019	0.045	0.040	9.09±0.25	0.014±0.002	2.29±0.19	0.039	0.033
F10b	0.35	12	34	47	20	24	11.09±0.23	0.018	0.042	0.036	11.21±0.25	0.050±0.018	9.85±5.34	0.041	0.036
F11	0.42	15	37	45	17	24	11.22±0.23	0.017	0.040	0.034	11.35±0.25	0.045±0.014	9.11±4.18	0.039	0.033
F12	0.43	18	42	47	18	24	7.34±0.46	0.019	0.044	0.039	7.48±0.35	0.035±0.012	5.33±2.16	0.043	0.038
F13	0.78	17	21	43	11	24	5.68±0.18	0.016	0.037	0.030	5.84±0.18	0.030±0.007	5.67±1.56	0.035	0.028
cont filament <sup>a</sup>	0.80			0.029±0.001				0.016	0.037	0.032	0.032±0.001	0.012±0.002	2.47±0.23	0.030	0.023
mean	0.65	22	32	45	18	24	6.84±0.18	0.020	0.046	0.041	7.03±0.20	0.033±0.009	5.24±1.78	0.045	0.039
median	0.53	16	29	43	17	24	7.32±0.18	0.019	0.045	0.039	7.37±0.21	0.027±0.006	4.64±1.32	0.042	0.037
minimum	0.27	4	14	40	11	24	0.03±0.001	0.015	0.036	0.029	0.03±0.001	0.012±0.002	1.84±0.17	0.030	0.023
maximum	1.37	82	64	65	36	25	11.22±0.46	0.031	0.074	0.071	11.35±0.35	0.081±0.030	10.05±5.74	0.066	0.062

Notes. (2) Filament length. (3) Filament mass. (4) Filament mass per unit length. (5) Total critical line-mass. (6) Nonthermal critical line-mass. (8) – (11) The amplitude, standard deviation  $\sigma = \text{FWHM}/(2\sqrt{2}\ln(2))$ , and width, and beam-deconvolved width derived from the Gaussian fitting. (12)–(16) The amplitude, flattening radius, density profile, width, and beam-deconvolved width derived from the Plummer fitting. a: the amplitude unit is  $\text{Jy beam}^{-1}$ .

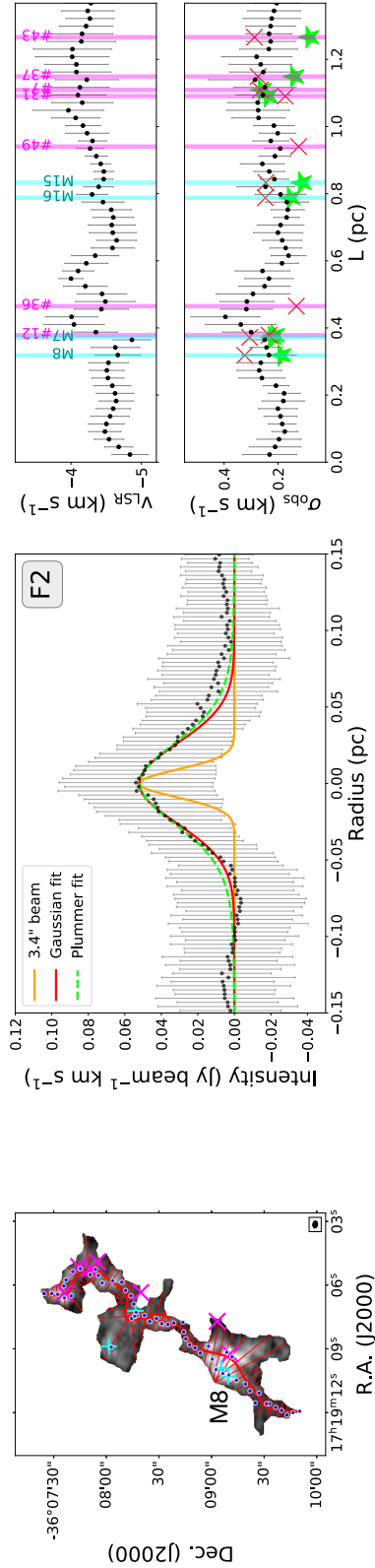


**Figure 13.** Left column: the filament spine (red solid curve) overlaid on the velocity-integrated intensity image. Magenta cross “x” and cyan plus “+” symbols are continuum cores and  $\text{NH}_2\text{D}$  cores, respectively. Middle column: mean integrated intensity profile and best-fit result (black dots) built by sampling radial cuts (short red solid lines) every 7 or 8 pixels ( $3''.44$  corresponds to  $\sim 0.019$  pc at the source distance of 1.3 kpc) along the spine. The radial distance is the projected distance from the peak emission at a given cut (blue dots in the left column). The error bar represents the standard deviation of the corresponding  $v_{\text{LSR}}$  and  $\sigma_{\text{obs}}$ . The orange solid line shows the beam response with a FWHM of  $\sim 3''.4$ . The red solid and green dashed lines present the best-fit results of Gaussian and Plummer fitting, respectively. Right column: the mean  $v_{\text{LSR}}$  and mean  $\sigma_{\text{obs}}$  of  $\text{H}^{13}\text{CO}^+$  line emission variation along the filament. The error bars show the standard deviation of corresponding  $v_{\text{LSR}}$  and  $\sigma_{\text{obs}}$ . Vertical magenta and cyan lines indicate the positions of associated continuum cores and  $\text{NH}_2\text{D}$  cores, respectively. The red cross “x” and green filled star symbols mark the core mean  $\sigma_{\text{obs}}$  derived from the  $\text{H}^{13}\text{CO}^+$  and  $\text{NH}_2\text{D}$  lines, respectively.

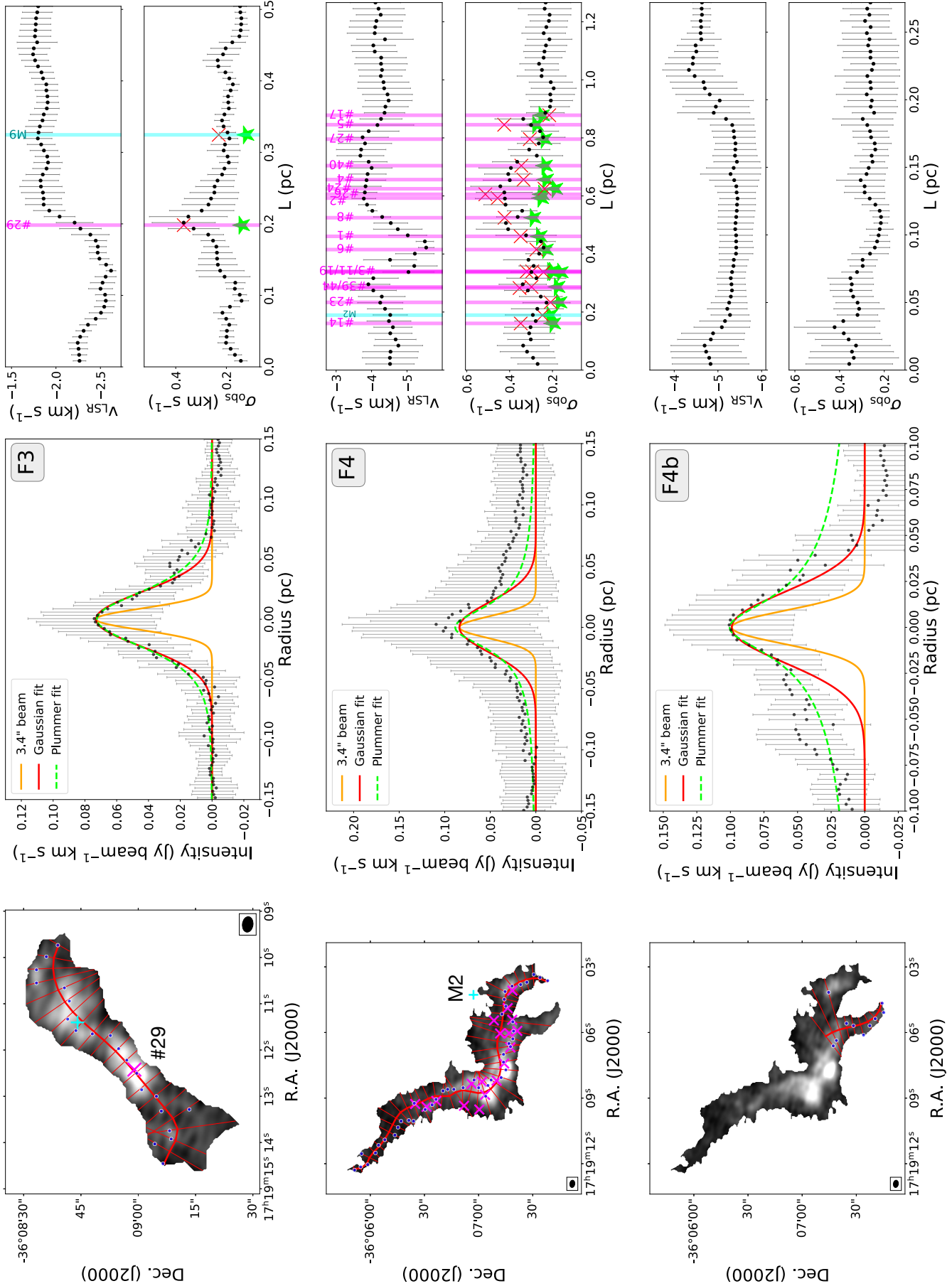


Figure 13.



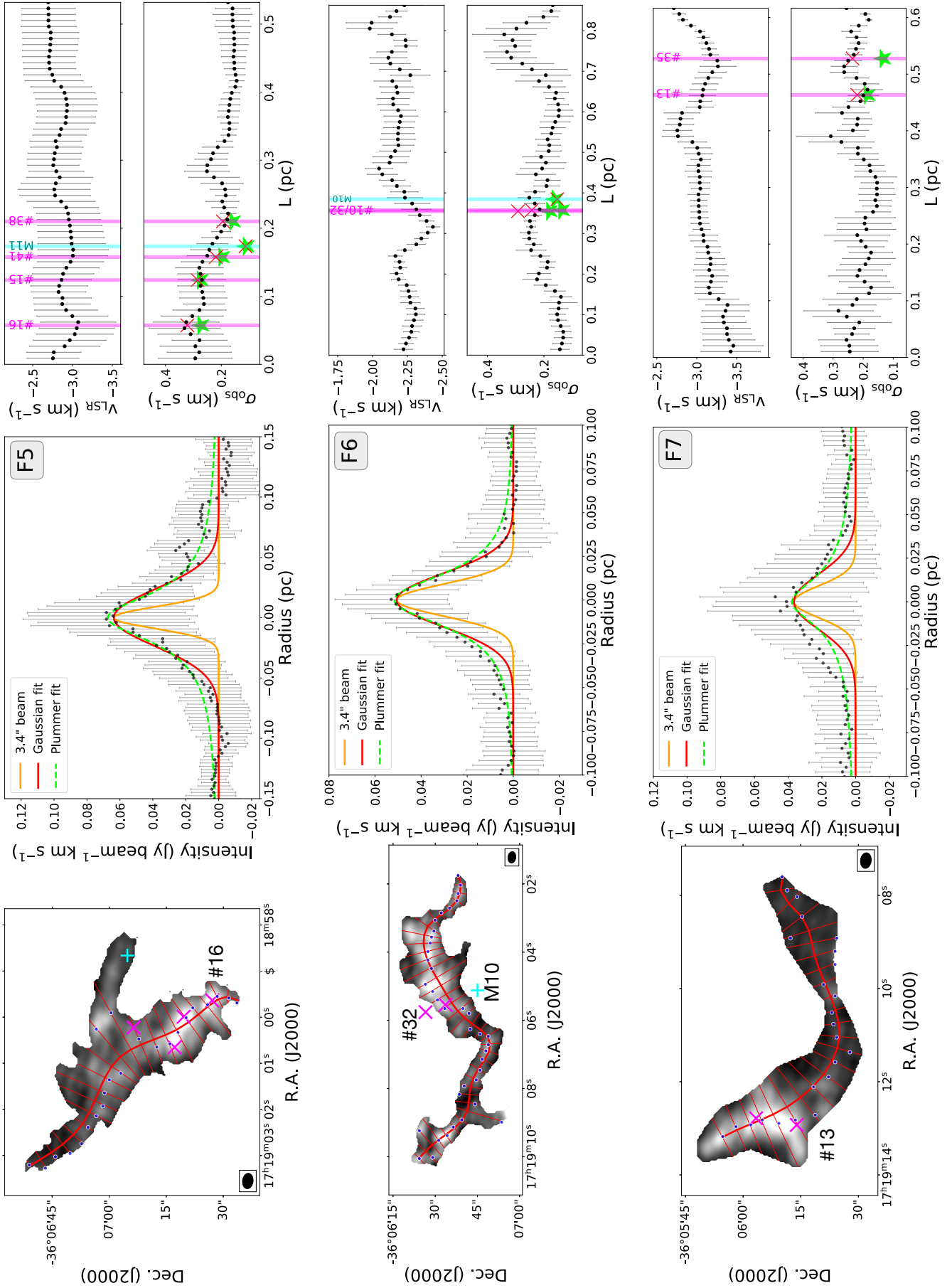


Figure 13.

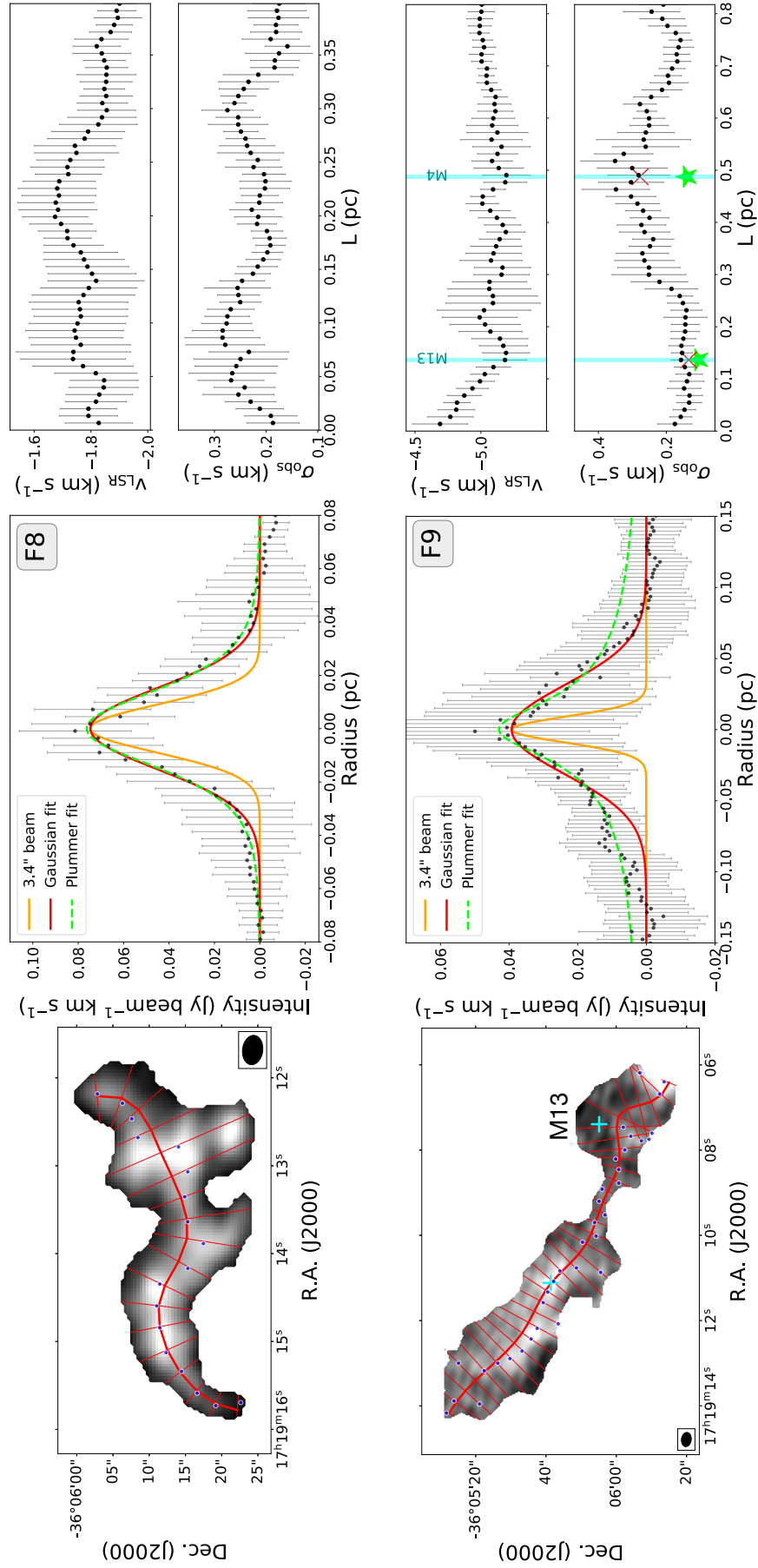


Figure 13.

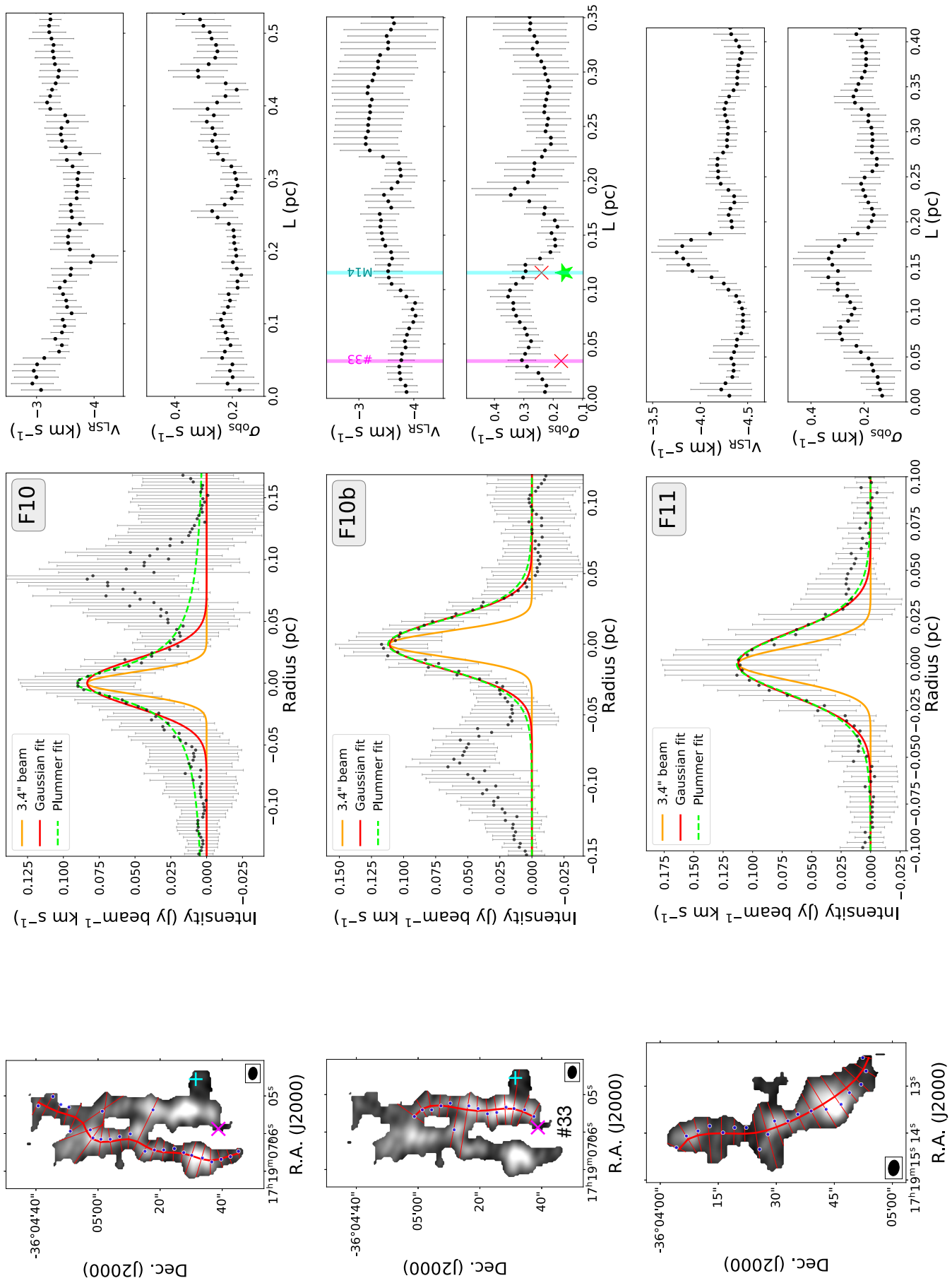


Figure 13.

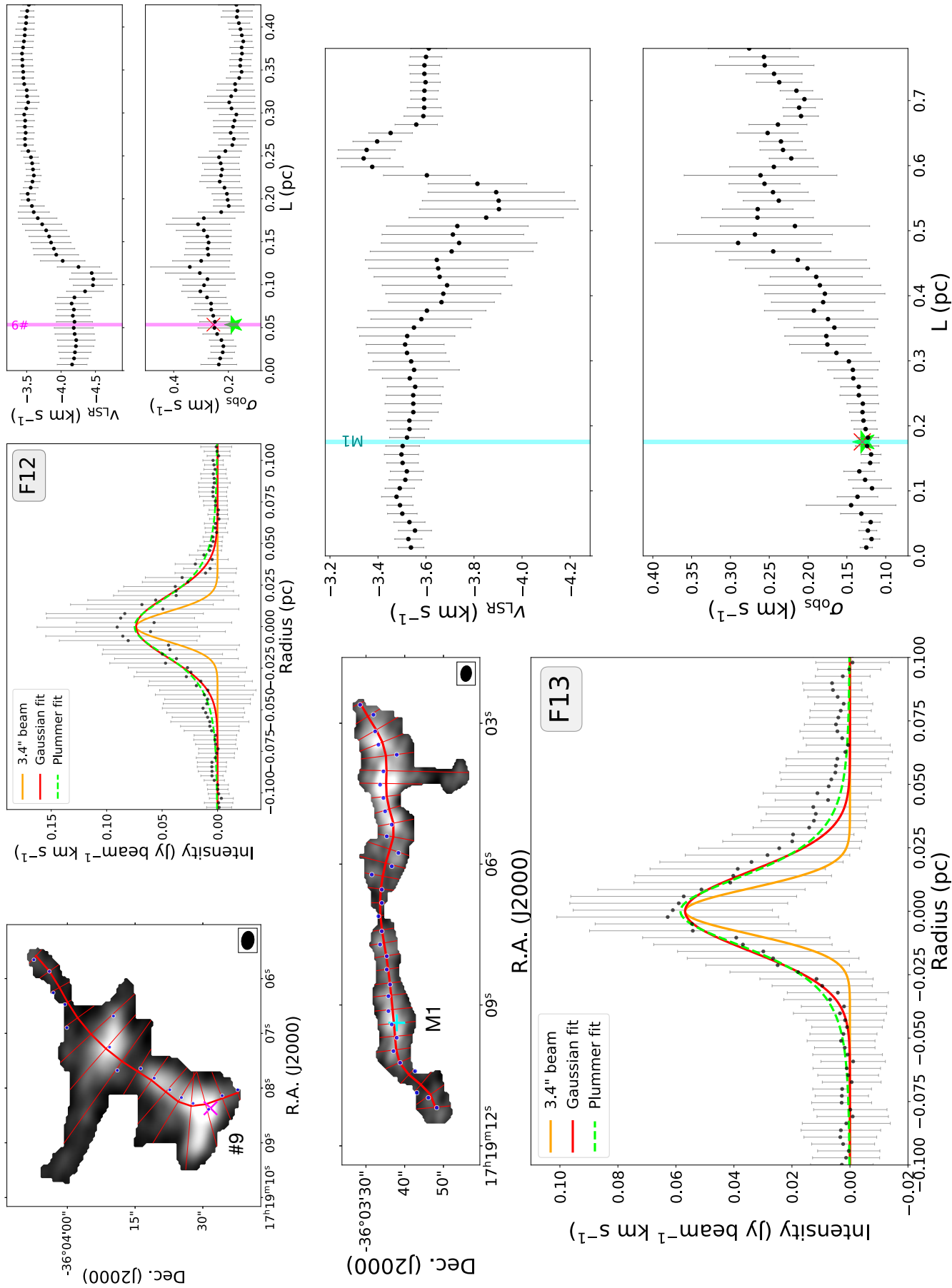


Figure 13.



## REFERENCES

- 932 André, P., Di Francesco, J., Ward-Thompson, D., et al.  
 933 2014, in *Protostars and Planets VI*, ed. H. Beuther, R. S.  
 934 Klessen, C. P. Dullemond, & T. Henning, 27,  
 935 doi: [10.2458/azu\\_uapress\\_9780816531240-ch002](https://doi.org/10.2458/azu_uapress_9780816531240-ch002)
- 936 André, P., Men'shchikov, A., Bontemps, S., et al. 2010,  
 937 *A&A*, 518, L102, doi: [10.1051/0004-6361/201014666](https://doi.org/10.1051/0004-6361/201014666)
- 938 Arzoumanian, D., André, P., Didelon, P., et al. 2011, *A&A*,  
 939 529, L6, doi: [10.1051/0004-6361/201116596](https://doi.org/10.1051/0004-6361/201116596)
- 940 Arzoumanian, D., André, P., Könyves, V., et al. 2019,  
 941 *A&A*, 621, A42, doi: [10.1051/0004-6361/201832725](https://doi.org/10.1051/0004-6361/201832725)
- 942 Astropy Collaboration, Robitaille, T. P., Tollerud, E. J.,  
 943 et al. 2013, *A&A*, 558, A33,  
 944 doi: [10.1051/0004-6361/201322068](https://doi.org/10.1051/0004-6361/201322068)
- 945 Beuther, H., Ragan, S. E., Johnston, K., et al. 2015, *A&A*,  
 946 584, A67, doi: [10.1051/0004-6361/201527108](https://doi.org/10.1051/0004-6361/201527108)
- 947 Busquet, G., Estalella, R., Palau, A., et al. 2016, *ApJ*, 819,  
 948 139, doi: [10.3847/0004-637X/819/2/139](https://doi.org/10.3847/0004-637X/819/2/139)
- 949 Butner, H. M., Lada, E. A., & Loren, R. B. 1995, *ApJ*, 448,  
 950 207, doi: [10.1086/175953](https://doi.org/10.1086/175953)
- 951 Chen, C.-Y., Mundy, L. G., Ostriker, E. C., Storm, S., &  
 952 Dhabal, A. 2020, *MNRAS*, 494, 3675,  
 953 doi: [10.1093/mnras/staa960](https://doi.org/10.1093/mnras/staa960)
- 954 Chen, H. H.-H., Pineda, J. E., Goodman, A. A., et al.  
 955 2019a, *ApJ*, 877, 93, doi: [10.3847/1538-4357/ab1a40](https://doi.org/10.3847/1538-4357/ab1a40)
- 956 Chen, H.-R. V., Zhang, Q., Wright, M. C. H., et al. 2019b,  
 957 *ApJ*, 875, 24, doi: [10.3847/1538-4357/ab0f3e](https://doi.org/10.3847/1538-4357/ab0f3e)
- 958 Chibueze, J. O., Omodaka, T., Handa, T., et al. 2014, *ApJ*,  
 959 784, 114, doi: [10.1088/0004-637X/784/2/114](https://doi.org/10.1088/0004-637X/784/2/114)
- 960 Chung, E. J., Lee, C. W., Kim, S., et al. 2019, *ApJ*, 877,  
 961 114, doi: [10.3847/1538-4357/ab12d1](https://doi.org/10.3847/1538-4357/ab12d1)
- 962 Churchwell, E., Babler, B. L., Meade, M. R., et al. 2009,  
 963 *PASP*, 121, 213, doi: [10.1086/597811](https://doi.org/10.1086/597811)
- 964 Clarke, S. D., Whitworth, A. P., Duarte-Cabral, A., &  
 965 Hubber, D. A. 2017, *MNRAS*, 468, 2489,  
 966 doi: [10.1093/mnras/stx637](https://doi.org/10.1093/mnras/stx637)
- 967 Contreras, Y., Garay, G., Rathborne, J. M., & Sanhueza, P.  
 968 2016, *MNRAS*, 456, 2041, doi: [10.1093/mnras/stv2796](https://doi.org/10.1093/mnras/stv2796)
- 969 Contreras, Y., Sanhueza, P., Jackson, J. M., et al. 2018,  
 970 *ApJ*, 861, 14, doi: [10.3847/1538-4357/aac2ec](https://doi.org/10.3847/1538-4357/aac2ec)
- 971 Cox, N. L. J., Arzoumanian, D., André, P., et al. 2016,  
 972 *A&A*, 590, A110, doi: [10.1051/0004-6361/201527068](https://doi.org/10.1051/0004-6361/201527068)
- 973 Gerner, T., Beuther, H., Semenov, D., et al. 2014, *A&A*,  
 974 563, A97, doi: [10.1051/0004-6361/201322541](https://doi.org/10.1051/0004-6361/201322541)
- 975 Ginsburg, A., & Mirocha, J. 2011, *PySpecKit: Python*  
 976 *Spectroscopic Toolkit*, *Astrophysics Source Code Library*.  
 977 <http://ascl.net/1109.001>
- 978 Gómez, G. C., & Vázquez-Semadeni, E. 2014, *ApJ*, 791,  
 979 124, doi: [10.1088/0004-637X/791/2/124](https://doi.org/10.1088/0004-637X/791/2/124)
- 980 Gómez, G. C., Vázquez-Semadeni, E., & Palau, A. 2021,  
 981 *MNRAS*, 502, 4963, doi: [10.1093/mnras/stab394](https://doi.org/10.1093/mnras/stab394)
- 982 Gong, H., & Ostriker, E. C. 2011, *ApJ*, 729, 120,  
 983 doi: [10.1088/0004-637X/729/2/120](https://doi.org/10.1088/0004-637X/729/2/120)
- 984 Gong, Y., Belloche, A., Du, F. J., et al. 2021, *A&A*, 646,  
 985 A170, doi: [10.1051/0004-6361/202039465](https://doi.org/10.1051/0004-6361/202039465)
- 986 Goodman, A. A., Alves, J., Beaumont, C. N., et al. 2014,  
 987 *ApJ*, 797, 53, doi: [10.1088/0004-637X/797/1/53](https://doi.org/10.1088/0004-637X/797/1/53)
- 988 Hacar, A., Kainulainen, J., Tafalla, M., Beuther, H., &  
 989 Alves, J. 2016, *A&A*, 587, A97,  
 990 doi: [10.1051/0004-6361/201526015](https://doi.org/10.1051/0004-6361/201526015)
- 991 Hacar, A., & Tafalla, M. 2011, *A&A*, 533, A34,  
 992 doi: [10.1051/0004-6361/201117039](https://doi.org/10.1051/0004-6361/201117039)
- 993 Hacar, A., Tafalla, M., & Alves, J. 2017, *A&A*, 606, A123,  
 994 doi: [10.1051/0004-6361/201630348](https://doi.org/10.1051/0004-6361/201630348)
- 995 Hacar, A., Tafalla, M., Forbrich, J., et al. 2018, *A&A*, 610,  
 996 A77, doi: [10.1051/0004-6361/201731894](https://doi.org/10.1051/0004-6361/201731894)
- 997 Hacar, A., Tafalla, M., Kauffmann, J., & Kovács, A. 2013,  
 998 *A&A*, 554, A55, doi: [10.1051/0004-6361/201220090](https://doi.org/10.1051/0004-6361/201220090)
- 999 Harris, C. R., Millman, K. J., van der Walt, S. J., et al.  
 1000 2020, *Nature*, 585, 357, doi: [10.1038/s41586-020-2649-2](https://doi.org/10.1038/s41586-020-2649-2)
- 1001 Hartmann, L. 2002, *ApJ*, 578, 914, doi: [10.1086/342657](https://doi.org/10.1086/342657)
- 1002 Hartmann, L., & Burkert, A. 2007, *ApJ*, 654, 988,  
 1003 doi: [10.1086/509321](https://doi.org/10.1086/509321)
- 1004 Heitsch, F., Ballesteros-Paredes, J., & Hartmann, L. 2009,  
 1005 *ApJ*, 704, 1735, doi: [10.1088/0004-637X/704/2/1735](https://doi.org/10.1088/0004-637X/704/2/1735)
- 1006 Heitsch, F., Hartmann, L. W., Slyz, A. D., Devriendt, J.  
 1007 E. G., & Burkert, A. 2008, *ApJ*, 674, 316,  
 1008 doi: [10.1086/523697](https://doi.org/10.1086/523697)
- 1009 Hennebelle, P. 2013, *A&A*, 556, A153,  
 1010 doi: [10.1051/0004-6361/201321292](https://doi.org/10.1051/0004-6361/201321292)
- 1011 Henshaw, J. D., Caselli, P., Fontani, F., Jiménez-Serra, I.,  
 1012 & Tan, J. C. 2014, *MNRAS*, 440, 2860,  
 1013 doi: [10.1093/mnras/stu446](https://doi.org/10.1093/mnras/stu446)
- 1014 Henshaw, J. D., Jiménez-Serra, I., Longmore, S. N., et al.  
 1015 2017, *MNRAS*, 464, L31, doi: [10.1093/mnras/lfw154](https://doi.org/10.1093/mnras/lfw154)
- 1016 Hildebrand, R. H. 1983, *QJRAS*, 24, 267
- 1017 Hoq, S., Jackson, J. M., Foster, J. B., et al. 2013, *ApJ*, 777,  
 1018 157, doi: [10.1088/0004-637X/777/2/157](https://doi.org/10.1088/0004-637X/777/2/157)
- 1019 Huchra, J. P., & Geller, M. J. 1982, *ApJ*, 257, 423,  
 1020 doi: [10.1086/160000](https://doi.org/10.1086/160000)
- 1021 Hunter, J. D. 2007, *Computing in Science Engineering*, 9,  
 1022 90
- 1023 Inutsuka, S.-I., & Miyama, S. M. 1992, *ApJ*, 388, 392,  
 1024 doi: [10.1086/171162](https://doi.org/10.1086/171162)
- 1025 Jiménez-Serra, I., Caselli, P., Fontani, F., et al. 2014,  
 1026 *MNRAS*, 439, 1996, doi: [10.1093/mnras/stu078](https://doi.org/10.1093/mnras/stu078)
- 1027 Kainulainen, J., Hacar, A., Alves, J., et al. 2016, *A&A*, 586,  
 1028 A27, doi: [10.1051/0004-6361/201526017](https://doi.org/10.1051/0004-6361/201526017)

- 1029 Kauffmann, J., Bertoldi, F., Bourke, T. L., Evans, N. J., I.,  
1030 & Lee, C. W. 2008, *A&A*, 487, 993,  
1031 doi: [10.1051/0004-6361:200809481](https://doi.org/10.1051/0004-6361:200809481)
- 1032 Kirk, H., Myers, P. C., Bourke, T. L., et al. 2013, *ApJ*, 766,  
1033 115, doi: [10.1088/0004-637X/766/2/115](https://doi.org/10.1088/0004-637X/766/2/115)
- 1034 Könyves, V., André, P., Men'shchikov, A., et al. 2015,  
1035 *A&A*, 584, A91, doi: [10.1051/0004-6361/201525861](https://doi.org/10.1051/0004-6361/201525861)
- 1036 Kumar, M. S. N., Palmeirim, P., Arzoumanian, D., &  
1037 Inutsuka, S. I. 2020, *A&A*, 642, A87,  
1038 doi: [10.1051/0004-6361/202038232](https://doi.org/10.1051/0004-6361/202038232)
- 1039 Lai, D. 2000, *ApJ*, 540, 946, doi: [10.1086/309361](https://doi.org/10.1086/309361)
- 1040 Li, D., & Goldsmith, P. F. 2012, *ApJ*, 756, 12,  
1041 doi: [10.1088/0004-637X/756/1/12](https://doi.org/10.1088/0004-637X/756/1/12)
- 1042 Li, G.-X., Urquhart, J. S., Leurini, S., et al. 2016, *A&A*,  
1043 591, A5, doi: [10.1051/0004-6361/201527468](https://doi.org/10.1051/0004-6361/201527468)
- 1044 Li, S., Zhang, Q., Pillai, T., et al. 2019a, *ApJ*, 886, 130,  
1045 doi: [10.3847/1538-4357/ab464e](https://doi.org/10.3847/1538-4357/ab464e)
- 1046 Li, S., Wang, J., Fang, M., et al. 2019b, *ApJ*, 878, 29,  
1047 doi: [10.3847/1538-4357/ab1e4c](https://doi.org/10.3847/1538-4357/ab1e4c)
- 1048 Li, S., Zhang, Q., Liu, H. B., et al. 2020a, *ApJ*, 896, 110,  
1049 doi: [10.3847/1538-4357/ab84f1](https://doi.org/10.3847/1538-4357/ab84f1)
- 1050 Li, S., Sanhueza, P., Zhang, Q., et al. 2020b, *ApJ*, 903, 119,  
1051 doi: [10.3847/1538-4357/abb81f](https://doi.org/10.3847/1538-4357/abb81f)
- 1052 Li, S., Lu, X., Zhang, Q., et al. 2021, *ApJL*, 912, L7,  
1053 doi: [10.3847/2041-8213/abf64f](https://doi.org/10.3847/2041-8213/abf64f)
- 1054 Lin, Y., Liu, H. B., Dale, J. E., et al. 2017, *ApJ*, 840, 22,  
1055 doi: [10.3847/1538-4357/aa6c67](https://doi.org/10.3847/1538-4357/aa6c67)
- 1056 Liu, H. B., Jiménez-Serra, I., Ho, P. T. P., et al. 2012, *ApJ*,  
1057 756, 10, doi: [10.1088/0004-637X/756/1/10](https://doi.org/10.1088/0004-637X/756/1/10)
- 1058 Liu, H.-L., Stutz, A., & Yuan, J.-H. 2018, *MNRAS*, 478,  
1059 2119, doi: [10.1093/mnras/sty1270](https://doi.org/10.1093/mnras/sty1270)
- 1060 —. 2019, *MNRAS*, 487, 1259, doi: [10.1093/mnras/stz1340](https://doi.org/10.1093/mnras/stz1340)
- 1061 Lu, X., Zhang, Q., Liu, H. B., et al. 2018, *ApJ*, 855, 9,  
1062 doi: [10.3847/1538-4357/aaad11](https://doi.org/10.3847/1538-4357/aaad11)
- 1063 Lu, X., Li, S., Ginsburg, A., et al. 2021, *ApJ*, 909, 177,  
1064 doi: [10.3847/1538-4357/abde3c](https://doi.org/10.3847/1538-4357/abde3c)
- 1065 Mac Low, M.-M. 1999, *ApJ*, 524, 169, doi: [10.1086/307784](https://doi.org/10.1086/307784)
- 1066 Mac Low, M.-M., & Klessen, R. S. 2004, *Reviews of Modern*  
1067 *Physics*, 76, 125, doi: [10.1103/RevModPhys.76.125](https://doi.org/10.1103/RevModPhys.76.125)
- 1068 Mangum, J. G., & Shirley, Y. L. 2015, *PASP*, 127, 266,  
1069 doi: [10.1086/680323](https://doi.org/10.1086/680323)
- 1070 McBreen, B., Fazio, G. G., Stier, M., & Wright, E. L. 1979,  
1071 *ApJL*, 232, L183, doi: [10.1086/183061](https://doi.org/10.1086/183061)
- 1072 McMullin, J. P., Waters, B., Schiebel, D., Young, W., &  
1073 Golap, K. 2007, in *Astronomical Society of the Pacific*  
1074 *Conference Series*, Vol. 376, *Astronomical Data Analysis*  
1075 *Software and Systems XVI*, ed. R. A. Shaw, F. Hill, &  
1076 D. J. Bell, 127
- 1077 Men'shchikov, A., André, P., Didelon, P., et al. 2010, *A&A*,  
1078 518, L103, doi: [10.1051/0004-6361/201014668](https://doi.org/10.1051/0004-6361/201014668)
- 1079 Miville-Deschênes, M. A., Martin, P. G., Abergel, A., et al.  
1080 2010, *A&A*, 518, L104,  
1081 doi: [10.1051/0004-6361/201014678](https://doi.org/10.1051/0004-6361/201014678)
- 1082 Miyama, S. M., Narita, S., & Hayashi, C. 1987, *Progress of*  
1083 *Theoretical Physics*, 78, 1051, doi: [10.1143/PTP.78.1051](https://doi.org/10.1143/PTP.78.1051)
- 1084 Molinari, S., Swinyard, B., Bally, J., et al. 2010, *A&A*, 518,  
1085 L100, doi: [10.1051/0004-6361/201014659](https://doi.org/10.1051/0004-6361/201014659)
- 1086 Monsch, K., Pineda, J. E., Liu, H. B., et al. 2018, *ApJ*, 861,  
1087 77, doi: [10.3847/1538-4357/aac8da](https://doi.org/10.3847/1538-4357/aac8da)
- 1088 Morii, K., Sanhueza, P., Nakamura, F., et al. 2021, *arXiv*  
1089 e-prints, arXiv:2109.01231.  
1090 <https://arxiv.org/abs/2109.01231>
- 1091 Müller, H. S. P., Schlöder, F., Stutzki, J., & Winnewisser,  
1092 G. 2005, *Journal of Molecular Structure*, 742, 215,  
1093 doi: [10.1016/j.molstruc.2005.01.027](https://doi.org/10.1016/j.molstruc.2005.01.027)
- 1094 Myers, P. C. 2009, *ApJ*, 700, 1609,  
1095 doi: [10.1088/0004-637X/700/2/1609](https://doi.org/10.1088/0004-637X/700/2/1609)
- 1096 Nagai, T., Inutsuka, S.-i., & Miyama, S. M. 1998, *ApJ*, 506,  
1097 306, doi: [10.1086/306249](https://doi.org/10.1086/306249)
- 1098 Nakamura, F., & Li, Z.-Y. 2008, *ApJ*, 687, 354,  
1099 doi: [10.1086/591641](https://doi.org/10.1086/591641)
- 1100 Nutter, D., Kirk, J. M., Stamatellos, D., &  
1101 Ward-Thompson, D. 2008, *MNRAS*, 384, 755,  
1102 doi: [10.1111/j.1365-2966.2007.12750.x](https://doi.org/10.1111/j.1365-2966.2007.12750.x)
- 1103 Ostriker, J. 1964, *ApJ*, 140, 1056, doi: [10.1086/148005](https://doi.org/10.1086/148005)
- 1104 Padoan, P., Juvela, M., Goodman, A. A., & Nordlund, Å.  
1105 2001, *ApJ*, 553, 227, doi: [10.1086/320636](https://doi.org/10.1086/320636)
- 1106 Padoan, P., Nordlund, Å., Kritsuk, A. G., Norman, M. L.,  
1107 & Li, P. S. 2007, *ApJ*, 661, 972, doi: [10.1086/516623](https://doi.org/10.1086/516623)
- 1108 Palmeirim, P., André, P., Kirk, J., et al. 2013, *A&A*, 550,  
1109 A38, doi: [10.1051/0004-6361/201220500](https://doi.org/10.1051/0004-6361/201220500)
- 1110 Peretto, N., Fuller, G. A., André, P., et al. 2014, *A&A*, 561,  
1111 A83, doi: [10.1051/0004-6361/201322172](https://doi.org/10.1051/0004-6361/201322172)
- 1112 Persi, P., & Tapia, M. 2008, *Star Formation in NGC 6334*,  
1113 ed. B. Reipurth, Vol. 5, 456
- 1114 Pineda, J. E., Goodman, A. A., Arce, H. G., et al. 2010,  
1115 *ApJL*, 712, L116, doi: [10.1088/2041-8205/712/1/L116](https://doi.org/10.1088/2041-8205/712/1/L116)
- 1116 Robitaille, T., & Bressert, E. 2012, *APLpy: Astronomical*  
1117 *Plotting Library in Python*, *Astrophysics Source Code*  
1118 *Library*. <http://ascl.net/1208.017>
- 1119 Russeil, D., Zavagno, A., Nguyen, A., et al. 2020, *A&A*,  
1120 642, A21, doi: [10.1051/0004-6361/202037674](https://doi.org/10.1051/0004-6361/202037674)
- 1121 Russeil, D., Schneider, N., Anderson, L. D., et al. 2013,  
1122 *A&A*, 554, A42, doi: [10.1051/0004-6361/201219971](https://doi.org/10.1051/0004-6361/201219971)
- 1123 Sanhueza, P., Jackson, J. M., Foster, J. B., et al. 2012,  
1124 *ApJ*, 756, 60, doi: [10.1088/0004-637X/756/1/60](https://doi.org/10.1088/0004-637X/756/1/60)
- 1125 —. 2013, *ApJ*, 773, 123, doi: [10.1088/0004-637X/773/2/123](https://doi.org/10.1088/0004-637X/773/2/123)
- 1126 Sanhueza, P., Jackson, J. M., Zhang, Q., et al. 2017, *ApJ*,  
1127 841, 97, doi: [10.3847/1538-4357/aa6ff8](https://doi.org/10.3847/1538-4357/aa6ff8)

- 1128 Sanhueza, P., Contreras, Y., Wu, B., et al. 2019, *ApJ*, 886,  
1129 102, doi: [10.3847/1538-4357/ab45e9](https://doi.org/10.3847/1538-4357/ab45e9)
- 1130 Sanhueza, P., Girart, J. M., Padovani, M., et al. 2021,  
1131 *ApJL*, 915, L10, doi: [10.3847/2041-8213/ac081c](https://doi.org/10.3847/2041-8213/ac081c)
- 1132 Sepúlveda, I., Estalella, R., Anglada, G., et al. 2020, *A&A*,  
1133 644, A128, doi: [10.1051/0004-6361/202037895](https://doi.org/10.1051/0004-6361/202037895)
- 1134 Smith, R. J., Glover, S. C. O., & Klessen, R. S. 2014,  
1135 *MNRAS*, 445, 2900, doi: [10.1093/mnras/stu1915](https://doi.org/10.1093/mnras/stu1915)
- 1136 Sokolov, V., Wang, K., Pineda, J. E., et al. 2018, *A&A*,  
1137 611, L3, doi: [10.1051/0004-6361/201832746](https://doi.org/10.1051/0004-6361/201832746)
- 1138 Soler, J. D., Beuther, H., Syed, J., et al. 2020, *A&A*, 642,  
1139 A163, doi: [10.1051/0004-6361/202038882](https://doi.org/10.1051/0004-6361/202038882)
- 1140 Stutz, A. M., & Gould, A. 2016, *A&A*, 590, A2,  
1141 doi: [10.1051/0004-6361/201527979](https://doi.org/10.1051/0004-6361/201527979)
- 1142 Tan, J. C., Kong, S., Butler, M. J., Caselli, P., & Fontani,  
1143 F. 2013, *ApJ*, 779, 96, doi: [10.1088/0004-637X/779/2/96](https://doi.org/10.1088/0004-637X/779/2/96)
- 1144 Treviño-Morales, S. P., Fuente, A., Sánchez-Monge, Á.,  
1145 et al. 2019, *A&A*, 629, A81,  
1146 doi: [10.1051/0004-6361/201935260](https://doi.org/10.1051/0004-6361/201935260)
- 1147 Van Loo, S., Keto, E., & Zhang, Q. 2014, *ApJ*, 789, 37,  
1148 doi: [10.1088/0004-637X/789/1/37](https://doi.org/10.1088/0004-637X/789/1/37)
- 1149 Vázquez-Semadeni, E., González-Samaniego, A., & Colín,  
1150 P. 2017, *MNRAS*, 467, 1313, doi: [10.1093/mnras/stw3229](https://doi.org/10.1093/mnras/stw3229)
- 1151 Wang, K., Testi, L., Ginsburg, A., et al. 2015, *MNRAS*,  
1152 450, 4043, doi: [10.1093/mnras/stv735](https://doi.org/10.1093/mnras/stv735)
- 1153 Wang, K., Zhang, Q., Testi, L., et al. 2014, *MNRAS*, 439,  
1154 3275, doi: [10.1093/mnras/stu127](https://doi.org/10.1093/mnras/stu127)
- 1155 Wang, Y., Beuther, H., Schneider, N., et al. 2020, *A&A*,  
1156 641, A53, doi: [10.1051/0004-6361/202037928](https://doi.org/10.1051/0004-6361/202037928)
- 1157 Whitworth, A., & Summers, D. 1985, *MNRAS*, 214, 1,  
1158 doi: [10.1093/mnras/214.1.1](https://doi.org/10.1093/mnras/214.1.1)
- 1159 Willis, S., Marengo, M., Allen, L., et al. 2013, *ApJ*, 778, 96,  
1160 doi: [10.1088/0004-637X/778/2/96](https://doi.org/10.1088/0004-637X/778/2/96)
- 1161 Yuan, J., Li, J.-Z., Wu, Y., et al. 2018, *ApJ*, 852, 12,  
1162 doi: [10.3847/1538-4357/aa9d40](https://doi.org/10.3847/1538-4357/aa9d40)
- 1163 Yue, N.-N., Li, D., Zhang, Q.-Z., et al. 2021, *Research in*  
1164 *Astronomy and Astrophysics*, 21, 024,  
1165 doi: [10.1088/1674-4527/21/1/24](https://doi.org/10.1088/1674-4527/21/1/24)
- 1166 Zhang, Q., Wang, Y., Pillai, T., & Rathborne, J. 2009,  
1167 *ApJ*, 696, 268, doi: [10.1088/0004-637X/696/1/268](https://doi.org/10.1088/0004-637X/696/1/268)
- 1168 Zucker, C., Battersby, C., & Goodman, A. 2015, *ApJ*, 815,  
1169 23, doi: [10.1088/0004-637X/815/1/23](https://doi.org/10.1088/0004-637X/815/1/23)
- 1170 Zucker, C., & Chen, H. H.-H. 2018, *ApJ*, 864, 152,  
1171 doi: [10.3847/1538-4357/aad3b5](https://doi.org/10.3847/1538-4357/aad3b5)

1172

## APPENDIX

1173

## A. COLUMN DENSITY

Assuming local thermodynamic equilibrium (LTE), the column density of molecules can be calculated following (Mangum & Shirley 2015)

$$N = C_\tau \frac{3h}{8\pi^3 R} \frac{Q_{\text{rot}}}{S\mu^2 g_u} \frac{\exp(\frac{E_u}{kT_{\text{ex}}})}{\exp(\frac{h\nu}{kT_{\text{ex}}}) - 1} (J_\nu(T_{\text{ex}}) - J_\nu(T_{\text{bg}}))^{-1} \int \frac{T_R dv}{f}, \quad (\text{A1})$$

where  $C_\tau = \tau/(1 - \exp(-\tau))$  is the optical depth correction factor,  $h$  is the Planck constant,  $S\mu^2$  is the line strength multiplied by the square of dipole moment,  $R$  is the line intensity,  $g_u$  is the statistical weight of the upper level,  $T_{\text{ex}}$  is the excitation temperature,  $T_{\text{bg}}$  is the back ground temperature,  $E_u$  is the energy of the upper state,  $\nu$  is the transition frequency,  $\int T_R dv$  is the velocity-integrated intensity,  $f$  is the filling factor, and  $Q_{\text{rot}}$  is the partition function. Here  $f$  is assumed to be 1 and the  $T_{\text{NH}_3}$  approximates the  $T_{\text{ex}}$  of molecular lines (see Section 3.1). Both  $\text{H}^{13}\text{CO}^+$  and  $\text{NH}_2\text{D}$  emission are generally optically thin. The  $\text{NH}_2\text{D}$  partition function is  $Q_{\text{rot}} = 0.73T_{\text{ex}}^{3/2} + 6.56$  that is the best-fit result from a fit to the partition function obtained from CDMS catalogues at the different excitation temperatures of 10–300 K (Müller et al. 2005), while the  $\text{H}^{13}\text{CO}^+$  partition function can be estimated from  $Q_{\text{rot}} \approx kT_{\text{ex}}/hB + 1/3$  that is a approximation for diatomic linear molecules (Mangum & Shirley 2015). For  $\text{NH}_2\text{D}$ , the molecular parameters are 15 for  $g_u$ ; 11.91 D for  $S\mu^2$ ; 20.68 K for  $E_u$ ; 85.926 GHz for  $\nu$ ; 1/2 for  $R$  that is the relative intensity of the main hyperfine transition with respect to the other hyperfine transitions. For  $\text{H}^{13}\text{CO}^+$ , the molecular parameters are 3 for  $g_u$ ; 15.21 D<sup>2</sup> for  $S\mu^2$ ; 15.21 K for  $E_u/k$ ; 86.754288 GHz for  $\nu$ ; 1 for  $R$ .

The  $N_{\text{H}_2}$  is derived from the continuum emission with

$$N_{\text{H}_2} = \eta \frac{S_\nu}{\Omega B_\nu(T_{\text{dust}}) \kappa_\nu \mu m_{\text{H}}}, \quad (\text{A2})$$

where  $\eta=100$  is the gas-to-dust ratio,  $S_\nu$  is the peak flux density,  $\Omega$  is the beam solid angle,  $m_{\text{H}}$  is the proton mass,  $\mu=2.8$  is the mean molecular weight of the interstellar medium (Kauffmann et al. 2008), and  $\kappa_\nu$  is the dust opacity at a frequency of  $\nu$ . We used  $\kappa_\nu = 0.235 \text{ cm}^{-2} \text{ g}^{-1}$  by assuming  $\kappa_\nu = 10(\nu/1.2\text{THz})^\beta \text{ cm}^{-2} \text{ g}^{-1}$  and  $\beta = 1.5$  (Hildebrand 1983).

1190

## B. FILAMENT CRITICAL LINE-MASS

Assuming the filament is an infinite self-gravitating isothermal cylinder in hydrostatic equilibrium, the critical line-mass of filament can be estimated by (Ostriker 1964)

$$M_{\text{crit}} = \frac{2\sigma_{\text{eff}}^2}{G}, \quad (\text{B3})$$

where  $\sigma_{\text{eff}}$  is the effective velocity dispersion and  $G$  is the gravitational constant. If the thermal gas pressure is the only force opposing gravity, the  $\sigma_{\text{eff}} = c_s$ . If the turbulence is the only force against gravity,  $\sigma_{\text{eff}} = \sigma_{\text{nth}}$ . If both thermal and turbulence supports are considered,  $\sigma_{\text{eff}} = \sqrt{\sigma_{\text{nth}}^2 + c_s^2}$ . In the last case, the Equation B3 can be written as (see also Hacar et al. 2018):

$$M_{\text{crit}}(T, \sigma_{\text{nth}}) = \frac{2c_s^2}{G} \left( 1 + \left( \frac{\sigma_{\text{nth}}}{c_s} \right)^2 \right). \quad (\text{B4})$$